Numerical VIV analysis of a single elastically-mounted cylinder: Comparison between 2D and 3D URANS simulations

Simone Martini, Mitja Morgut, Riccardo Pigazzini *

Department of Engineering and Architecture, University of Trieste, Piazzale Europa 1 34127 Trieste, Italy

ARTICLE INFO

Keywords:
VIV
URANS
CFD
OpenFOAM

ABSTRACT

In this paper the numerical simulations of the flow around an elastically-mounted circular cylinder with one degree of freedom (1-DOF) with small damping parameter and small mass ratio are presented. The simulations are performed for subcritical Reynolds numbers ($2.0 \cdot 10^3 < Re < 1.3 < 10^4$), using the URANS (Unsteady Reynolds Averaged Navier Stokes) approach in combination with the SST (Shear Stress Transport) turbulence model. The simulations are carried out on 3D as well as 2D meshes. From the overall results it seems that the bi-dimensional approach could be effectively applied in the lower branch, while major discrepancies are present in the upper branch. The detailed analysis of the wake flow characteristics shows that the three dimensionality of the flow is stronger in the transition zones between the different branches. The extensive comparison between the computational simulations and the experimental results presented in this paper could be considered the "start point" in order to select the proper grid model depending on the requested accuracy.

1. Introduction

The problem of Vortex Induced Vibrations (VIV) on circular cylinders arises in many fields of engineering. Among others, coastal and marine applications such as pipe risers, mooring lines, spar, TLPs etc.

Vortex Induce Vibrations (VIV) has been studied also to develop renewable energy technology, using one or more oscillating cylinders in tandem configuration to generate electricity, see the VIVACE (Vortex Induced Vibration Aquatic Clean Energy) converter (Bernitsas et al., 2008).

VIV occurs when shedding vortices induce an oscillatory force on a blunt structure in steady or unsteady flow mostly in the direction perpendicular to the flow. If the structure is free to move or is partially restrained by *equivalent springs*, the body starts oscillating. Large oscillations are typically observed if the structure is subjected to near-resonance excitation. This occurs when there is the quasi-synchronization between vortex shedding frequency and natural frequency of the system. In such conditions the amplitude may be of the same order of the size of the body, depending on several parameters. The stiffness of the restoring mechanism, the mechanical damping, mass ratio and Reynolds number being some of them.

To understand, predict and prevent VIV phenomenon, a large amount of research has been carried out. Many of the studies concerning VIV are summarized in the comprehensive review of Gabbai and Benaroya (2005), Williamson and Govardhan (2008), Bearman (2011) and Sarpkaya (2004).

* Corresponding author.
E-mail addresses: simone.martini@phd.units.it (S. Martini), mmorgut@units.it (M. Morgut), riccardo.pigazzini@phd.units.it (R. Pigazzini).

One of the fundamental experimental campaign on an elastically mounted cylinder with very low mass and damping ratios was conducted by Khalak and Williamson (1996). Khalak and Williamson conducted the experiments at the Cornell-ONR free-surface water channel using an elastically-mounted vertical surface-piercing cylinder. The entire set of flow velocities has been obtained with a smooth continuous increment from the lowest to the highest value of the reduced velocity, U^*. A fixed flat horizontal plate was installed at $0.04D$ distance from the bottom of the cylinder in order to minimize 3D effects. This particular experimental set-up allowed the results to be used as a benchmark for the 2D simulations.

VIV is an extremely complex phenomenon, where large variations of the response of the cylinder are observed even for small variations of the incident flow velocity. In the particular case of low mass to displaced mass ratio (mass ratio m^*) the typical behaviour of the amplitude A of the motion of the cylinder with the increasing incident flow velocity is characterized by different branches, namely:

- initial branch, where A grows rapidly with U starting from very low values;
- upper branch, where A reaches its maximum value;
- lower branch, where A show a plateau.
- desynchronization region, where A tends towards low values.

A comprehensive review on the fluctuating lift on a cylinder at rest has been given by Norberg (2003), with focus on effects of Re. The representative time record of the lift force, the spectra, the root-mean-square value of lift and the pressure distribution on the cylinder surface are presented in order to understand three-dimensional features on the flow field as consequence of the Re variation.

VIV of a circular cylinder has been investigated in many numerical studies, several CFD results comes from 2D simulation studies with different turbulence models: Guilmineau and Queutey (2004), (Pan et al., 2007), Wanderley et al. (2008), (Wu et al., 2014) and Pigazzini et al. (2018a,b). Due to the lack of 3D effects, the results of those studies could do not match experimental data.

Since the vortex wake of the high-Re flow around circular cylinders is in general three-dimensional, several 3D numerical studies have been conducted.

At the present, due to the difficulties connected with the expensive hardware capacity and extra modelling efforts required to properly describe the fluid flow beyond the laminar region, the vast majority of 3D VIV simulations of circular cylinders in literature are concerned with low-Re flows.

Among others, Blackburn et al. (2001), presented a comparison between the results from experiments, bi- and three-dimensional direct numerical simulations (DNS) of vortex-induced vibration at low-Re. The three-dimensional simulations matched the experiments well, whereas no amplitude branches were observed for the two-dimensional simulations. This led to the conclusion that bi-dimensional simulations are inadequate for modelling high-Re vortex-induced vibration (VIV). The operational problems emerged, on both sides, related to the difficulties in obtaining high-Re values in the DNS simulation, on one hand, and low values of Re in experiments, on the other, have highlighted the limitations of this comparison between the numerical and the experimental results.

D. Lucor (2005) presented results of a direct numerical simulation of 1-DOF VIV for three different Reynolds numbers: Re = 1000, 2000 and 3000. They noticed the dependence of the location and magnitude of upper branch response on Re. They also found that there is a sharp drop in the spanwise correlation factor of wake and forces in the region of U^* around the transition between the upper and lower branches, and confirmed the existence of a hysteretic region between this two branches.

Leontini et al. (2006) investigated the response behaviour of a 1-DOF VIV of 3D cylinder subjected to VIV at Re = 200. Their numerical study contribute to understanding of the previous discrepancies about the low-Re and the high-Re VIV behaviour. Two response branches similar to the upper and lower branches at high-Re were discovered. Therefore, they concluded that the mechanism that causes the upper and lower branches is not a product of three-dimensionality of the flow (high-Re), although it may be amplified by three-dimensionality.

Zhao et al. (2014) studied the transition from 2D to 3D for 1-DOF VIV of a circular cylinder at Re ranging from 150 to 1000. In their study, the three-dimensionality of the flow appeared to be strongest in the upper branch and weakest in the initial branch. But, for both 2D and 3D simulations, the predicted peak vibration amplitudes are around $0.7\,D$ although the experiments, conducted at higher Reynolds number, show amplitudes well over $1.0\,D$.

Application of low-Re simulations is arguable, since the flow around marine structures, which present submerged cylindrical structures (pipe and cables), is in general in the range $10^4 < Re < 10^6$. Therefore, thanks also to the growing of the computational resources, the numerical study of the VIV phenomenon at higher Reynolds number has become of greater interest.

One of the first attempts of a 3D numerical simulation of a cylinder self excited oscillations at high-Re is found in the work of Saltara et al. (2011).

Saltara used the Spalart–Allmaras Detached Eddy Simulation (DES) to simulate 1-DOF VIV of a circular cylinder with a low mass-damping parameter at Re = 10^4. In general, their simulation results partially agreed with the experimental results of Khalak and Williamson (Khalak and Williamson, 1996). The vibration amplitudes and force coefficients follow the three response branches defined by different ranges of the reduced velocity, but were overpredicted for $U^* > 6$.

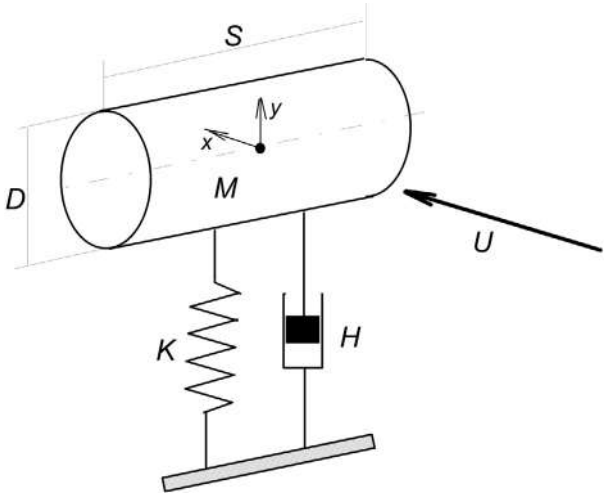

Fig. 1. Schematic representation of VIV problem and relevant symbols.

Furthermore, the shift in phase angle between lift coefficient and cylinder displacement, obtained in the simulations, occurs at a different reduced velocity respect to the experiments.

The use of the bi-dimensional approach may easily reduce the computational time by a few orders of magnitude, but since the three dimensionality of the flow is an important issue for VIV, 3D simulation are necessary in order to correctly capture the physics of the problem (Shur et al., 2005).

Thus, in this work, we explore the applicability of 2D simulations to predict VIV phenomenon in different branches. In addition, we assess the accuracy of 2D and 3D simulations carried out with the considered approach by comparing numerical results with experimental data.

The test case used in the present paper is the 1-DOF VIV of a circular cylinder with low mass and damping ratios, published by Khalak and Williamson (1996). The numerical simulations are carried out using the URANS solver available in OpenFOAM an open-source CFD toolbox (version 2.4).

The present paper shows how the wake flow of a circular cylinder subject to VIV is essentially bi-dimensional in the lower branch. The strongest flow variation along the cylinder span have been found in transitions between a branch and another and in the desynchronization region. The lowest correlation factors are found to occur in the transitional and desynchronization regimes. The vortex shedding patterns are also analysed and it compares well to the Willamson–Rosko map (Williamson and Roshko, 1988).

The paper is organized as follows.

The test case used as reference data is introduced in Section 2.

In Section 3 a description of the CFD simulations is given.

The results obtained from the simulations are discussed in Section 4. In particular, after a comparison of the cylinder response between the CFD results and the experimental data, the variation of sectional lift coefficient in time among the axial direction of cylinder is presented. Then, a careful analysis of vortex shedding modes and the phase between the motion of the cylinder and the lift force is presented.

2. Problem description

In this work we consider a circular cylinder of mass M, with a diameter D and span S, free to move in transverse direction respect to a uniform cross flow U. The cylinder is considered mounted on a linear spring and a weak linear damper. The system in question is sketched in Fig. 1 where the spring stiffness and the mechanical damping of the system are identified with K and H, respectively.

The dimensionless dynamic parameters, considered in this study, are those of the experimental set-up of Khalak and Williamson (1996). The experimental studies were characterized by low mass ratio $m^* = M/(\rho\pi D^2 S/4) = 2.4$ and low damping ratio $\zeta = H/H_{critical} \approx 0.0054$. $H_{critical}$ is the standard critical damping of a linear mass–spring–damper system. Further definitions and details are listed in Table 1.

In this study the reduced velocity $U^* = U/(f_0 D)$, where f_0 is the natural frequency of the system in still fluid, was systematically varied from 2 to 17 by changing the uniform (free-stream) cross flow velocity U. This range of reduced velocity corresponds to sub-critical Reynolds numbers in the range of $2.0 \cdot 10^3$ to $1.4 \cdot 10^4$.

Table 1
System properties.

Description	Symbol	Value	
Cylinder diameter	D (m)	0.0381	
Mass ratio	$m^* = M/(\rho \frac{\pi D^2}{4} S)$	2.4000	
Damping Ratio	$\zeta = H/(2\sqrt{K(M + M_A)})$	0.0054	
Added mass coefficient	$C_A = M_A/(\rho \frac{\pi D^2}{4} S)$	1.0000	
Mass-damping parameter	$m^* \zeta$	0.0130	
Natural frequency in air	$f_{0,a} = \frac{1}{2\pi}\sqrt{\frac{K}{M}}$ (Hz)	0.7846	
Natural frequency in water	$f_0 = \frac{1}{2\pi}\sqrt{\frac{K}{M+M_A}}$ (Hz)	0.6592	
		2D	3D
Cylinder span	S (m)	0.0250	0.3800
Cylinder mass	M (kg)	0.0683	1.0388
Spring stiffness	K (N/m)	1.6609	25.2465
Structural damping	H (N/(m/s))	0.0043	0.0660

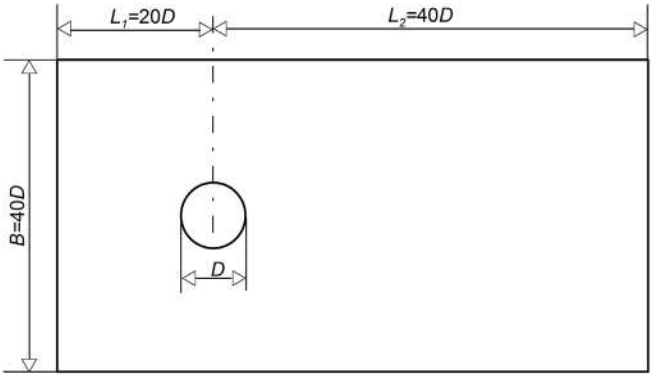

Fig. 2. Slice of computational domain.

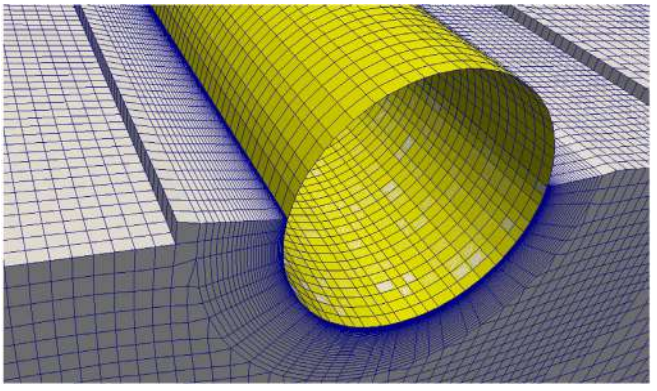

Fig. 3. Details of the grid refinement in the near wall region.

3. Simulations setup

The numerical simulations were performed using OpenFOAM (OF) library (release 2.4), an open source finite volume based CFD (Computational Fluid Dynamics) toolbox. The URANS approach was used and the workhorse SST (Shear Stress Transport) turbulence model (namely $k - \omega$ SST in OF), with $y^+ \approx 1$, was employed in order to close the system of the governing equations.

The simulations were carried out on 3D and 2D meshes. Here, it is important to clarify that the 2D meshes are intended as 3D meshes with only one layer of cells normal to the XY plane. The 3D meshes were generated by extruding the corresponding 2D meshes. The number of cells and refinement were determined by a preliminary mesh independence

study. The final computational mesh had 38188 cells for the 2D case, with a single cell in the direction perpendicular to the XY plane; whereas the 3D one has a cell count of 3479859, with 255 cells along the span direction of the cylinder. The final span-wise resolution of the 3D mesh respected the guidelines suggested by D'Alessandro et al. (2016), suggesting a minimum number of 48 cells every πD to capture the streamwise vortex structures. In Fig. 2 the computational domain, in the XY plane view, is depicted. The cylinder span was defined according to Khalak and Williamson (1996) (i.e. $S \approx 10D$) for the 3D case. Fig. 3 shows an horizontal clip of the 3D mesh, where the boundary layer grading close to the cylinder surface and the cells size along the span are shown.

Free-stream velocity, constant static pressure and no-slip condition were used on the Inlet, Outlet and Body boundary conditions respectively. The coupling between the rigid body motion and the fluid flow is explicit. ALE method was used to follow the mesh motion (Löhner and Yang, 1996), the displacement of the internal nodes was computed from the boundary motions by means of the Laplace equation with variable diffusivity based on inverse distance. The linear upwind scheme was used for the discretization of the advective terms while the first order implicit Euler method, coupled with the dynamically adjustable stepping technique (Lysenko et al., 2014), was used for time integration. To achieve stable and convergent calculations for every time step, a Courant number Co less than 0.9 was adopted.

The overall simulations were performed using fresh water. Full details of the boundary and initial conditions used for the velocity, pressure, turbulent kinetic energy k and the turbulence specific dissipation rate ω are provided in detail in Pigazzini et al. (2018a) for convenience.

4. Results and discussion

In this section the results of the CFD simulations are discussed. The differences between the bi-dimensional and three-dimensional URANS simulations are highlighted. The cylinder VIV response is presented in terms of motion amplitude and frequency, then the analysis of total and vortex forces and their phases respect to the cylinder motion are discussed. In this study the tree-dimensional character of the wake field is illustrated using different plots and evaluated using the correlation coefficient. Finally the vortex flow patterns are compared to the well known Roshko map (Williamson and Roshko, 1988). Computational costs and facilities are then briefly summarized.

4.1. Cylinder response

The results from current 3D VIV simulations are compared with both experimental data by Khalak and Williamson (1996) and results corresponding to the 2D simulations. The cylinder response is shown in terms of non-dimensional amplitude $A^* = A/D$ and its non-dimensional frequency $f^* = f/f_0$ in Fig. 4(a) and Fig. 4(b) respectively.

3D simulations show good agreement with experimental results in terms of response amplitude both in the initial and the upper branch. The greatest discrepancies between CFD and experimental results are found in the upper branch and in the transition zone between lower branch and desyncronization regime. Otherwise, the oscillation amplitudes are in reasonable agreement with experimental results.

The difference in the upper–lower branch transition location between CFD ($U^* = 6$) and experimental results ($U^* \approx 7$), may be due to the distinction of velocity initial conditions between the two methods. Indeed, the velocity initial condition for the CFD simulation was fixed at the target value for every case, while in the experiments, the velocity was gradually incremented. Lower branch amplitudes are slightly underestimated between $U^* = 6$ and $U^* = 8$. This effect has been also observed by Morse et al. (2008) in the case of attached endplate (as in the simulations) compared to experimental data from Khalak and Williamson (1999).

Comparing 2D and 3D results in Fig. 4(a), the most important difference lies in the better estimation of maximum oscillation amplitudes in the upper branch using the 3D URANS approach, as well as in the desyncronization range for $U^* \geq 15$. Notable differences are also observed in the initial part of desyncronization range.

The cylinder frequency response of 2D and 3D simulations compares very well with experimental data in Fig. 4(b). In particular, also some double-peaked behaviour in the initial branch has been successfully simulated. The frequency response of the 3D simulations in the upper branch shows slightly lower frequencies in respect to experimental results, otherwise a good agreement with experimental data is found. In Fig. 4(b), it can also be seen that the dominant frequency of 2D simulations and experiments increases throughout the upper branch, where in the case of 3D simulation, the frequency stays near the natural frequency instead. This particular aspect is commented in the next section.

4.2. Force coefficient and phase

In an attempt to further investigate the vortex shedding modes obtained with the numerical simulations, an additional analysis was made on the phase lag between the motion of the cylinder and the forcing term. In that respect, Williamson and Govardhan (2004) suggest to consider not only the total force F_L but also the "vortex shedding" (VS) force F_{VS} thus, following the decomposition used by Govardhan and Williamson (2000) the vortex shedding force can be computed by

$$F_{VS}(t) = F_L(t) - F_{POT}(t) \tag{1}$$

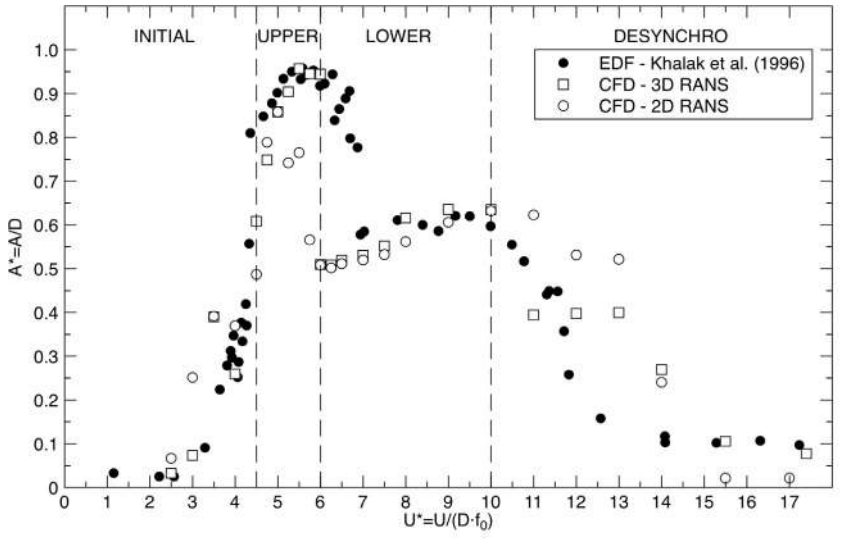

(a)

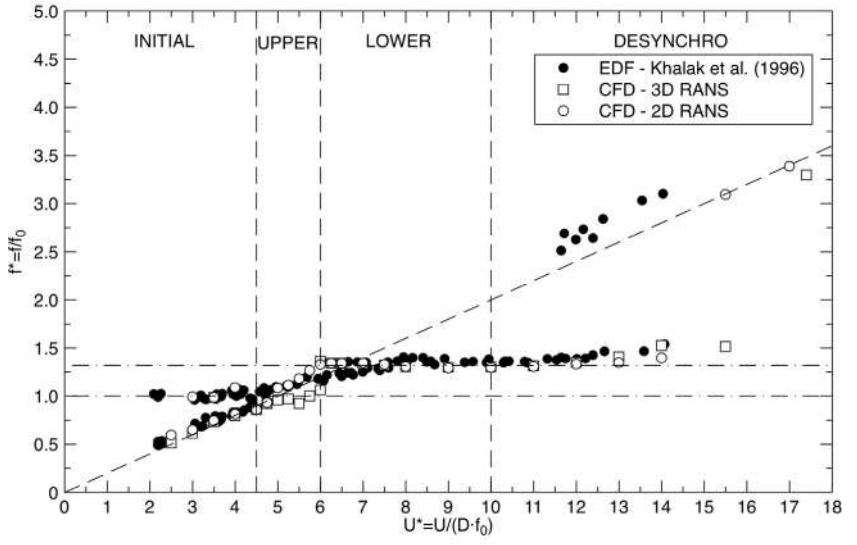

(b)

Fig. 4. Amplitude ratio $A^* = A/D$ (a) and frequency ratio $f^* = f/f_0$ (b) versus reduced velocity U^*. Comparison between experimental data by Khalak and Williamson (1996) (solid circles), present 2D CFD results (empty circles) and present 3D CFD results (empty squares). Vertical dashed lines marks the boundaries of branches in accordance with the CFD results. The oblique dashed line in (b) corresponds to St = 0.20.

F_{POT} is the potential force component, given by the potential added-mass force:

$$F_{POT}(t) = -M_A\ddot{y} \tag{2}$$

with $M_A = C_A\rho\frac{\pi D^2}{4}S$ is the added mass, C_A the added mass coefficient.

In non-dimensional form, F_L, F_{VS} and F_{POT} can be written conveniently as:

$$C_L(t) = \frac{F_L}{F_0}, \qquad C_{VS}(t) = \frac{F_{VS}}{F_0}, \qquad C_{POT}(t) = \frac{F_{POT}}{F_0}, \tag{3}$$

where $F_0 = \frac{1}{2}\rho DSU^2$ is a reference force.

The root mean square (rms) of the total force C_L amplitude and phase ϕ between the total force and the displacement are presented in Fig. 5(a) with respect to the reduced velocity U^* for both 2D and 3D simulations.

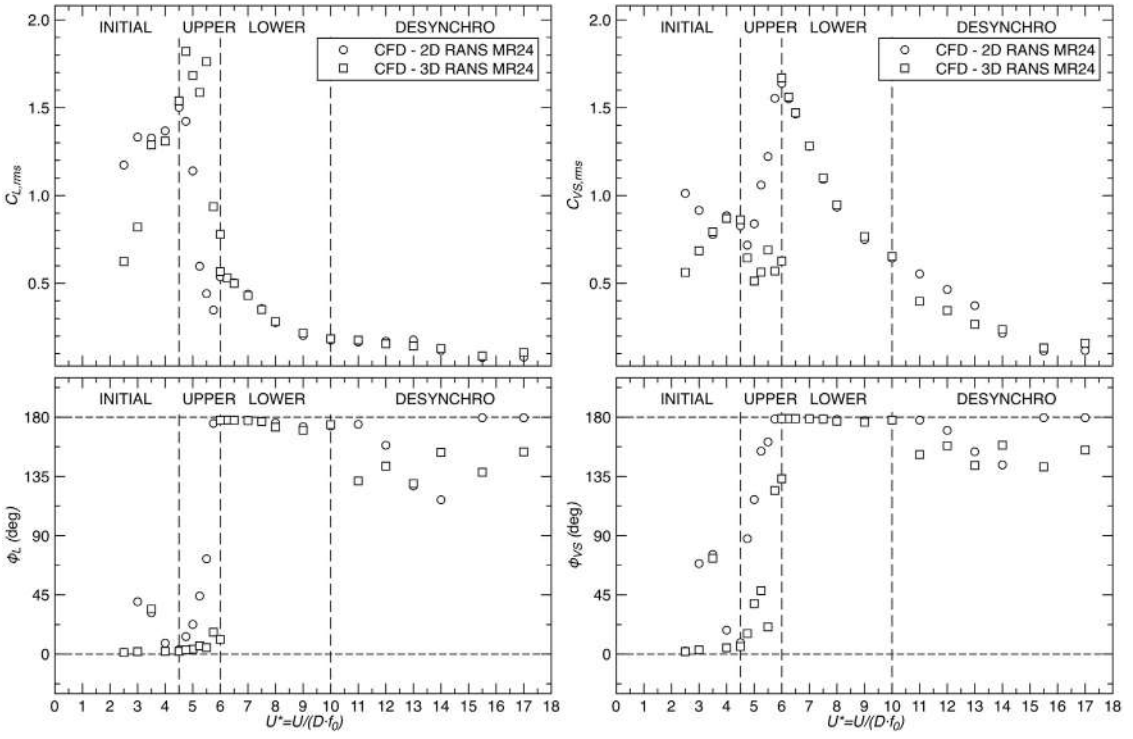

(a) Total force. (b) Vortex Shedding force.

Fig. 5. Force and phase angle variation with U^*.

The total force shows a rapid increase in its amplitude between the initial and upper branch, where it peaks. A sharp drop is shown in the upper–lower transition zone as expected (see Govardhan and Williamson, 2000). The total force further decreases along the lower branch an desynchronization regime.

Differences between 2D and 3D are most visible in the initial and upper branches: in the early stages of initial branch, 2D simulations show higher total force, where in the upper branch it drops rapidly, where the 3D case shows higher and more steady values. In general, the 3D case shows higher total force in the upper branch respect to the 2D case, allowing for larger amplitudes. No significant differences are present both in the lower branch and desynchronization regime as 2D and 3D results overlap.

The total force phase ϕ comparison shows that the 3D case exhibit a sharp jump of the total force phase jump between upper and lower branch, from 0 to 180 deg as observed, and reported in Khalak and Williamson (1999). The 2D results show instead that during the upper branch, the phase rise gradually before reaching 180 deg a little earlier than the 3D case. Total force phases of both cases remain almost identical in the lower branch.

The value of the vortex shedding force, C_{VS}, and phase, ϕ_{VS}, between the vortex shedding force and the displacement are presented in Fig. 5(b). Also for the case of the vortex shedding force, the main differences between the two cases are found in the upper branch. Differently from what observed in the case of the total force, the vortex shedding force of the 3D case is lower and more constant compared to the 2D case. Also, the vortex shedding force in the 2D case rises in the upper branch peaking at the upper–lower transition. For the 3D case, vortex shedding force in the upper branch is lower than the total force. The 2D case instead shows values of the vortex shedding forces that are higher than the total force towards the end of the upper branch. For $U^* \geq 5$, the vortex shedding force is almost identical for both cases in the lower branch, the 3D case shows slightly lower values once in the desynchronization range.

The vortex shedding force ϕ_{VS} phase shows that in both 2D and 3D cases in the upper branch there are intermediate values between 0 and 180 deg. No large phase jump is present between upper and lower branch, both cases show increasing phase angle, and as in the case for the total force, the 2D case reaches 180 deg phase slightly earlier than the 3D case. Also in this case, phases in the lower branch are identical.

Fig. 6 shows the non-dimensional time domain vortex shedding force C_{VS} and the non-dimensional total force C_L, obtained through the 2D and the 3D CFD simulations respectively, for eight representative flow regimes ($U^* = 3.5, 4.5, 5, 5.5, 5.75, 6, 6.25, 12$). In the same figures, the non-dimensional cylinder displacement $y(t)/D$ time series are also shown. The bottom plot of Fig. 6 shows also the phase $\phi(t)$ as function of time computed using the Hilbert transform (Williamson and Govardhan, 2004).

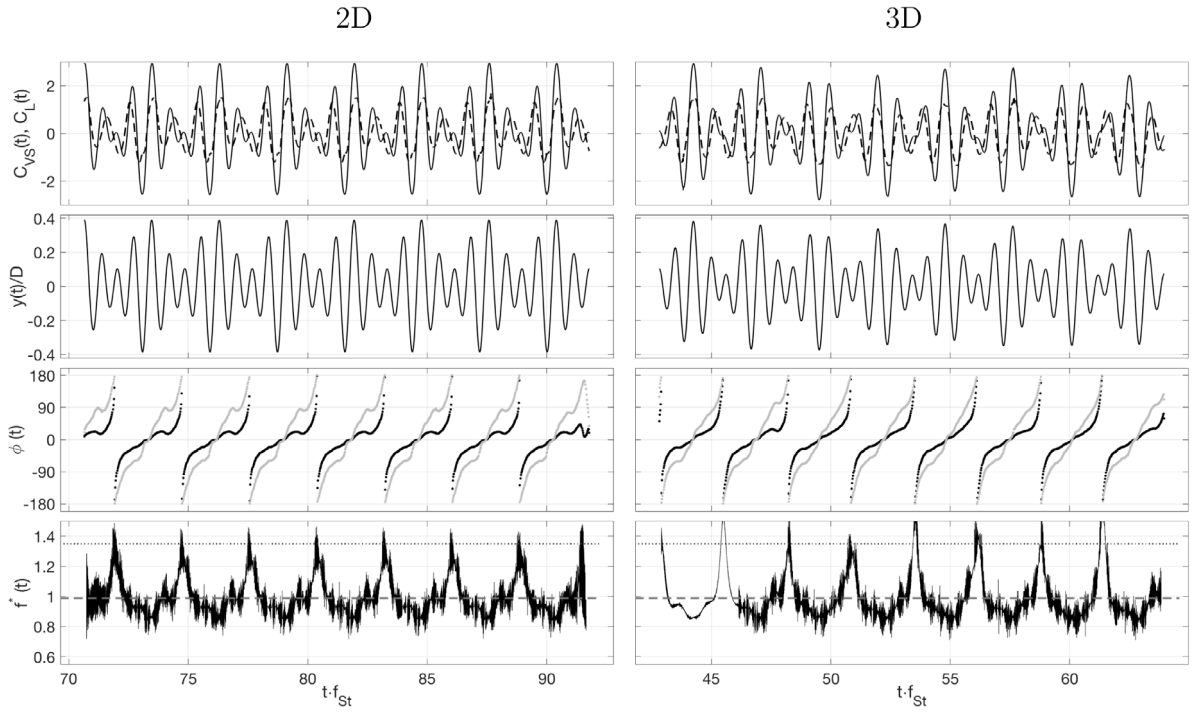

(a) Initial branch, Re=2941, U^*=3.50

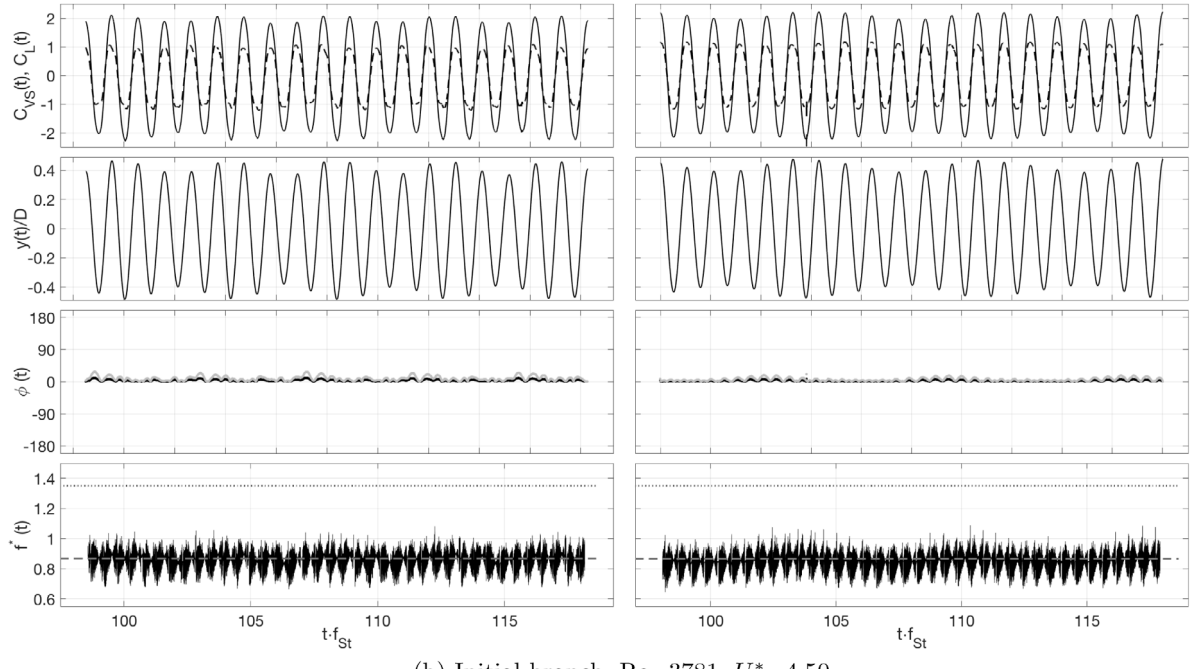

(b) Initial branch, Re=3781, U^*=4.50

Fig. 6. First plot: total $C_L(t)$ (solid line) and vortex shedding force coefficient $C_{VS}(t)$ (dashed line). Second plot: non-dimensional cylinder displacement $y(t)$. Third plot: phase angle ϕ_L between C_L and $y(t)$ (black points) and phase angle ϕ_{VS} between C_{VS} and $y(t)$ (grey points). Fourth plot: frequency ratio $f^*(t)$ (using Hilbert transform), dashed line shows the main oscillation frequency (from analysis of spectral peaks) and dotted line shows the synchronization frequency at lower branch.

As noted by Williamson and Govardhan (2004) the initial excitation regime can be marked by two sub-regimes. The first sub-regime denoted as "quasi-periodic" (QP) exhibits "slipping" of the phase angle $\phi(t)$ periodically through 360°. As shown in Fig. 6(a), the QP sub-regime is well captured by both 2D and 3D URANS simulations.

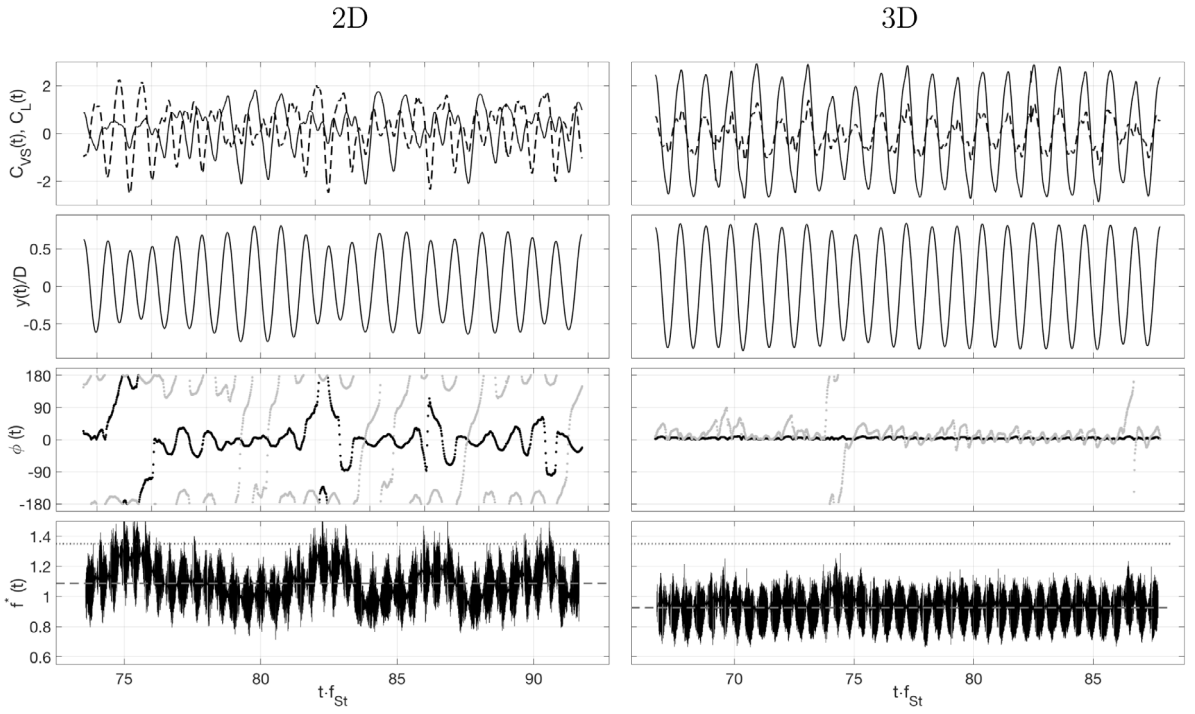

(c) Upper branch, Re=4202, U^*=5.00

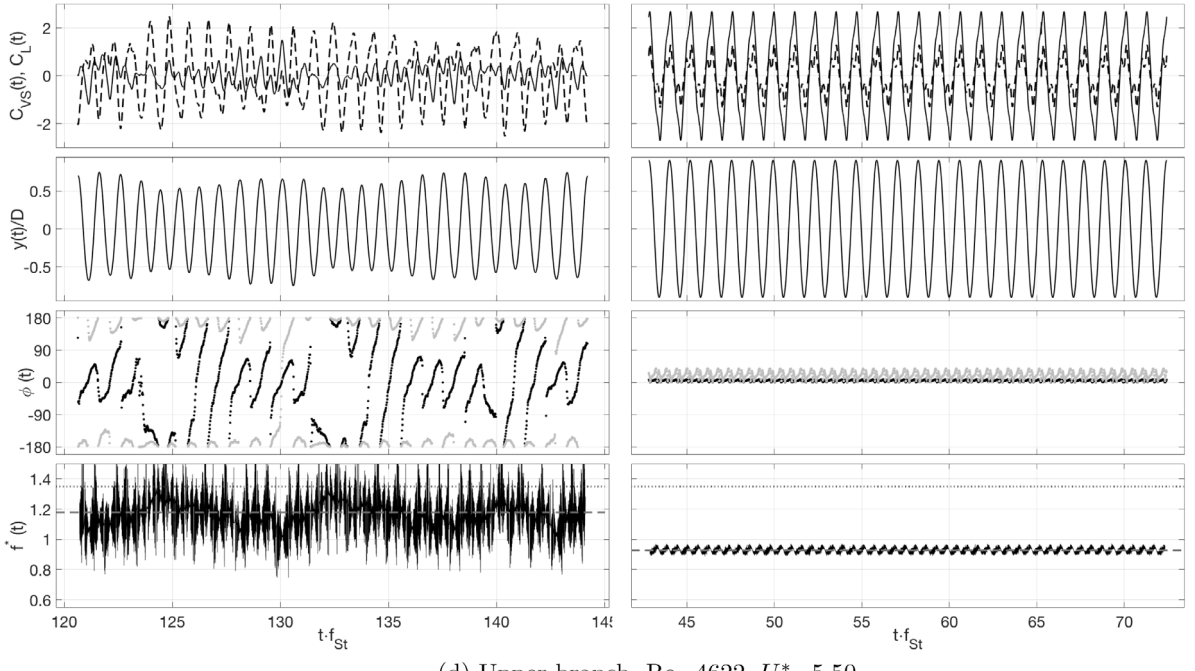

(d) Upper branch, Re=4622, U^*=5.50

Fig. 6. (*continued*).

The second sub-regime denoted as "periodic" (P) instead, shows a constant phase angle $\phi(t)$ which remains close to 0°. In this initial branch the vortex shedding phase ϕ_{VS} follows the trend of the total phase angle $\phi(t)$. Again there is a perfect correspondence between the 2D and 3D simulation and the experimental data (see Fig. 6(b)).

The main observation for what concerns the upper branch is that the 2D time series appear to be less stable. It can be seen in Figs. 6(c) and 6(d) that the instantaneous phase and frequency ratios of the left plots are unsteady whereas

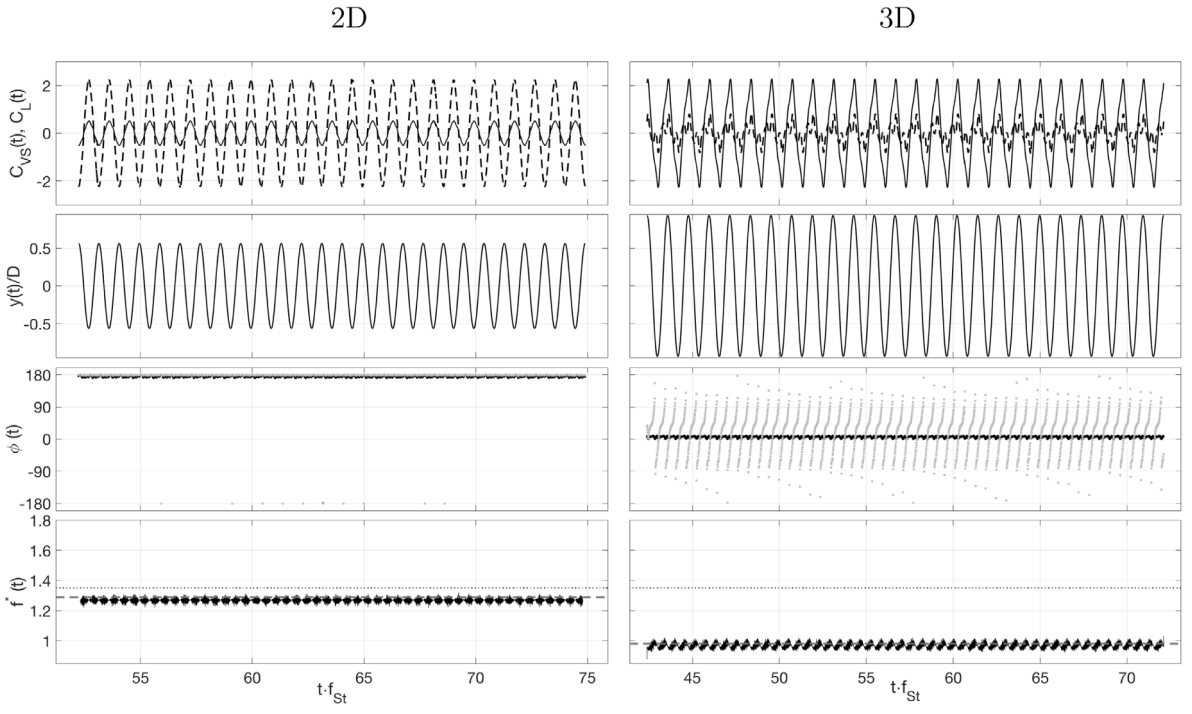

(e) Upper branch, Re=4832, U^*=5.75

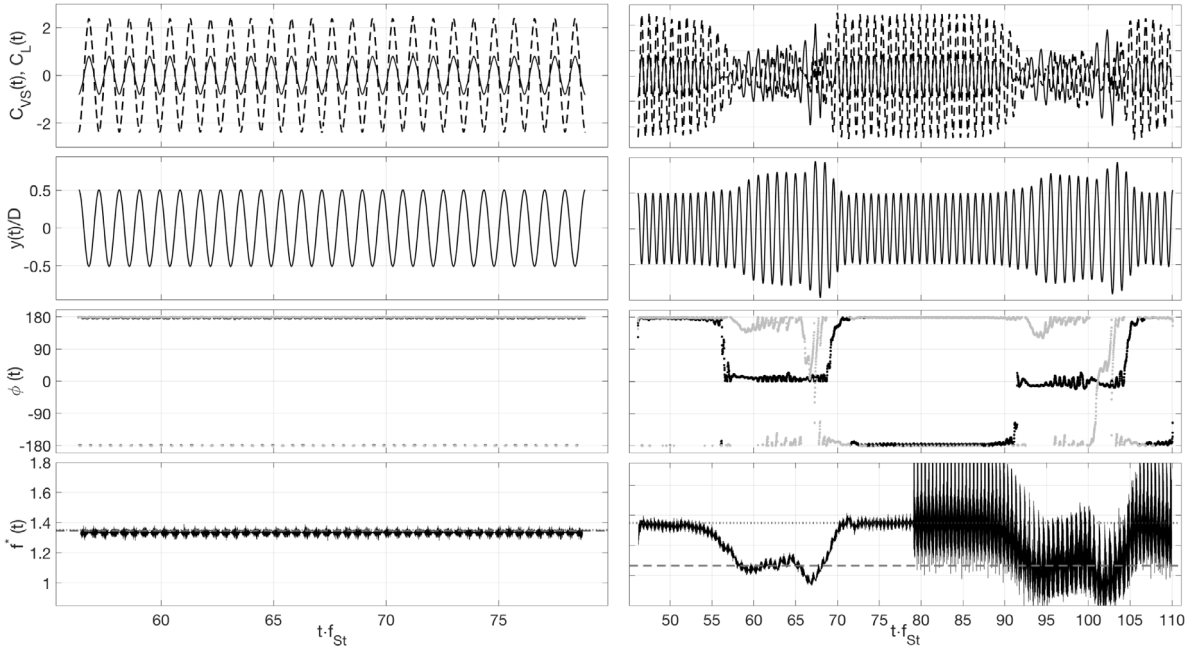

(f) Transition upper/lower branch, Re=5042, U^*=6.00

Fig. 6. (*continued*).

on the right plots a steady value has been achieved. The frequency response unsteadiness for such low mass ratio m^* has been observed by Govardhan and Williamson during experiments (Govardhan and Williamson, 2000). It is worth noting that as the phase of the 2D results tends to zero for a some time (see Fig. 6(c) left plot around $80 \cdot t_{St}$), also frequency ratio tends to the same values observed in 3D results, and the maximum 2D motion amplitude occurs.

The fact that the frequency for the 2D case during the upper branch is not steady means that the value of the frequency ratio plotted in Fig. 4(b) (obtained using spectral peak analysis) is an average value, that is never steadily achieved by

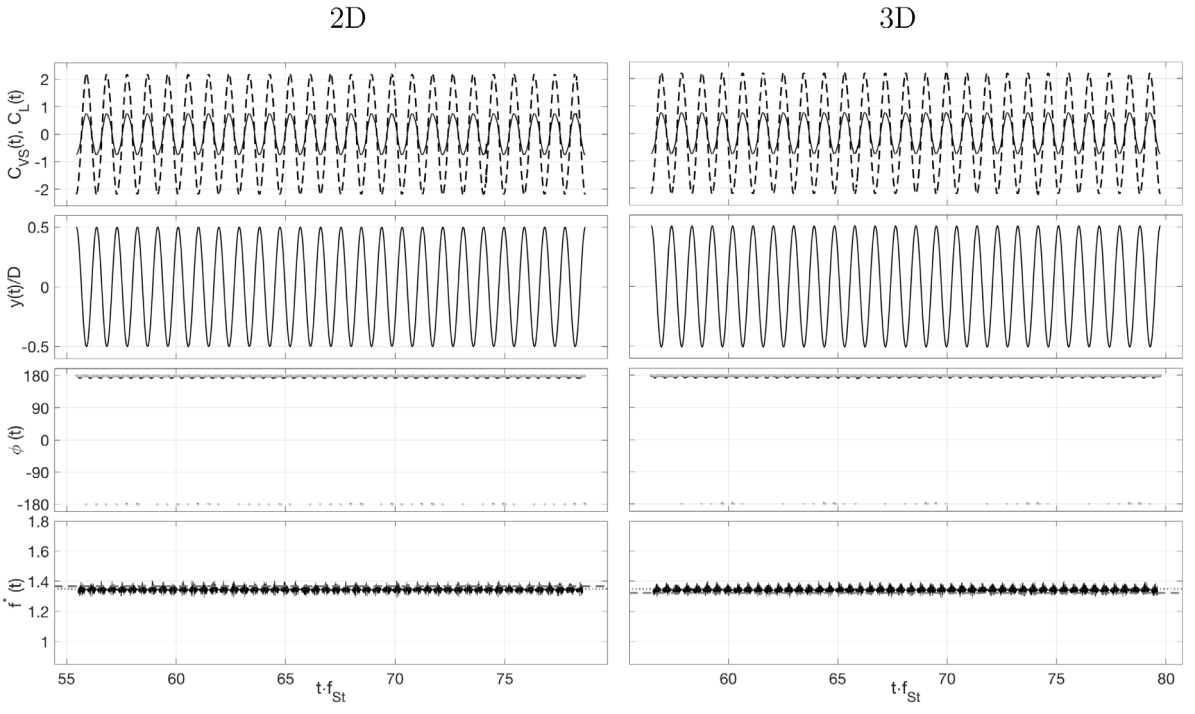

(g) Lower branch, Re=5252, U^*=6.25

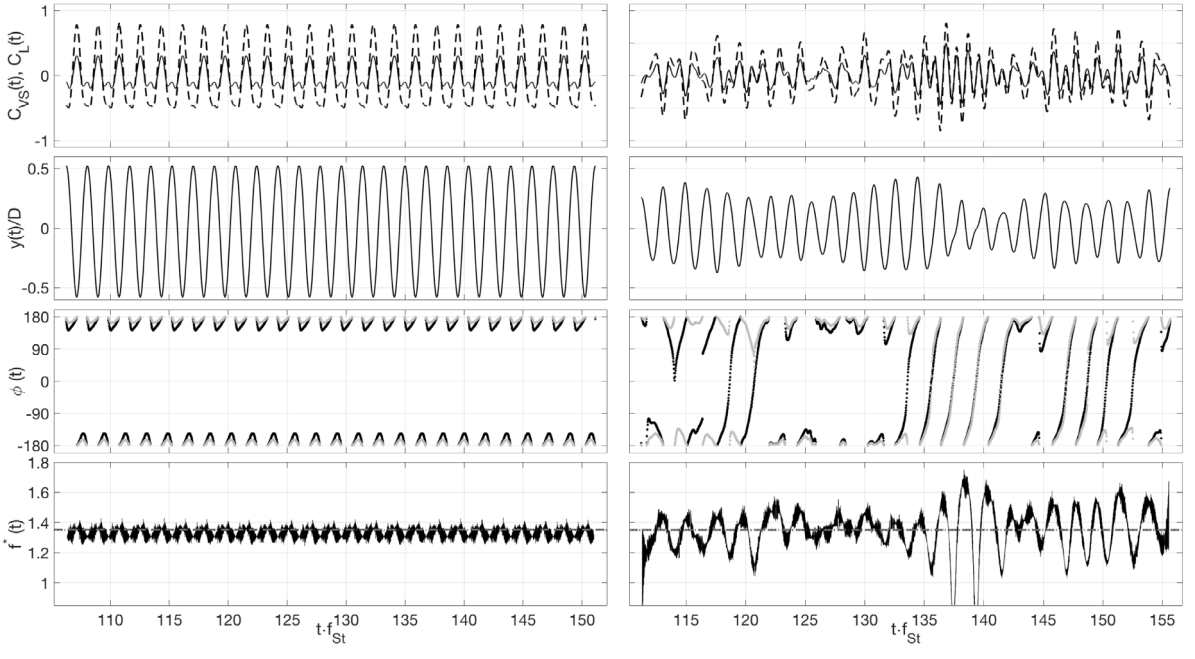

(h) Deshyncronization regime, Re=10084, U^*=12.00

Fig. 6. (*continued*).

the simulations. Differently, the frequency ratio of 3D simulations obtained using the Hilbert transform is equal to the spectral peak frequency through the entire window.

As noted above, the change of vortex shedding mode is associated with the start of the synchronization phase $U^* = 6$. The jump of the total phase $\phi(t)$ is clearly visible in the 2D case already at $U^* = 5.75$ (Fig. 6(e) left), while the 3D case remains in the upper branch. Intermittent behaviour is observed only in the 3D case for $U^* = 6$ (Fig. 6(f) right). The

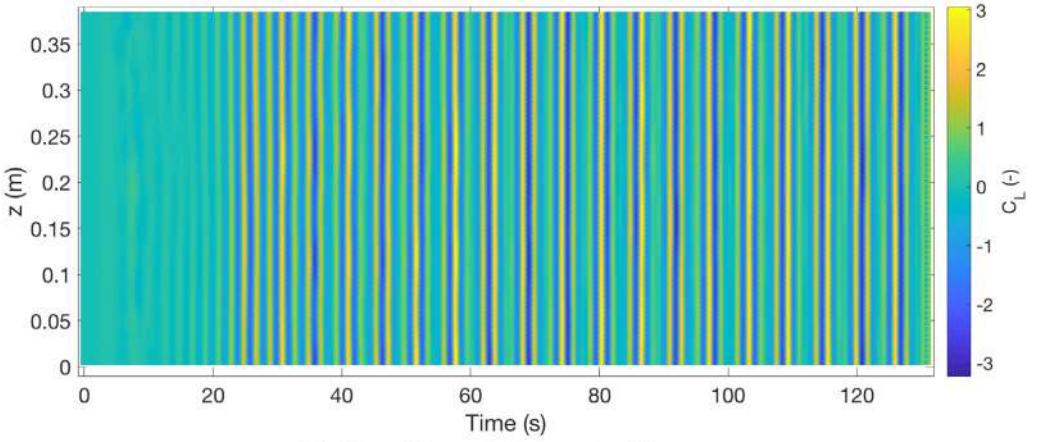

(a) Initial branch, Re=2941, U^*=3.50

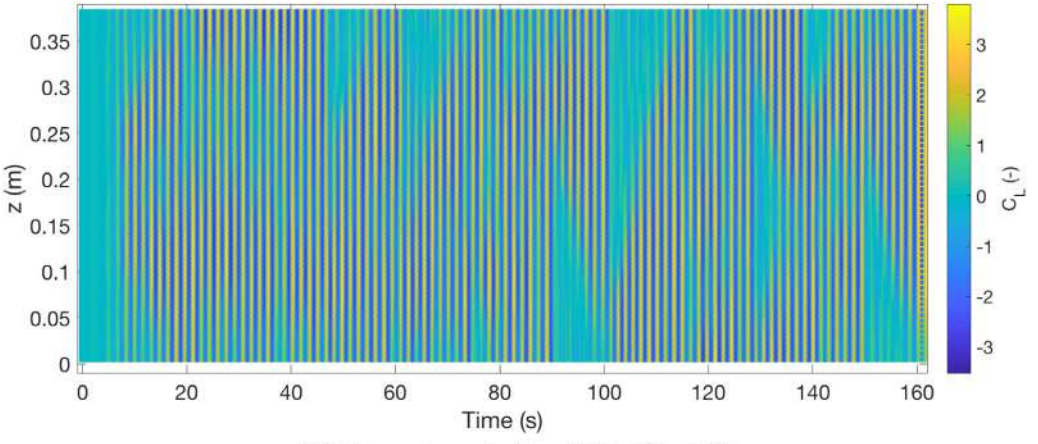

(b) Upper branch, Re=4202, U^*=5.00

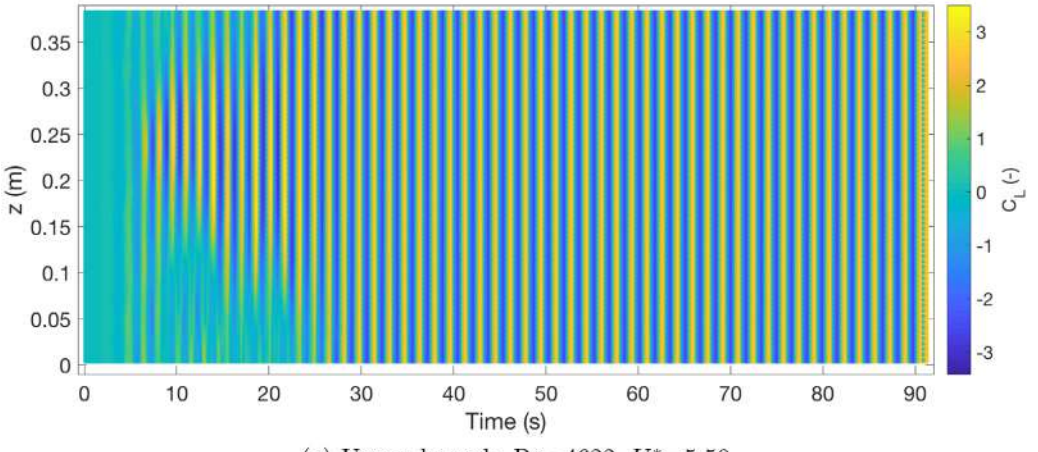

(c) Upper branch, Re=4622, U^*=5.50

Fig. 7. Contours of the lift coefficient on the z-t plane for the 3D URANS cases.

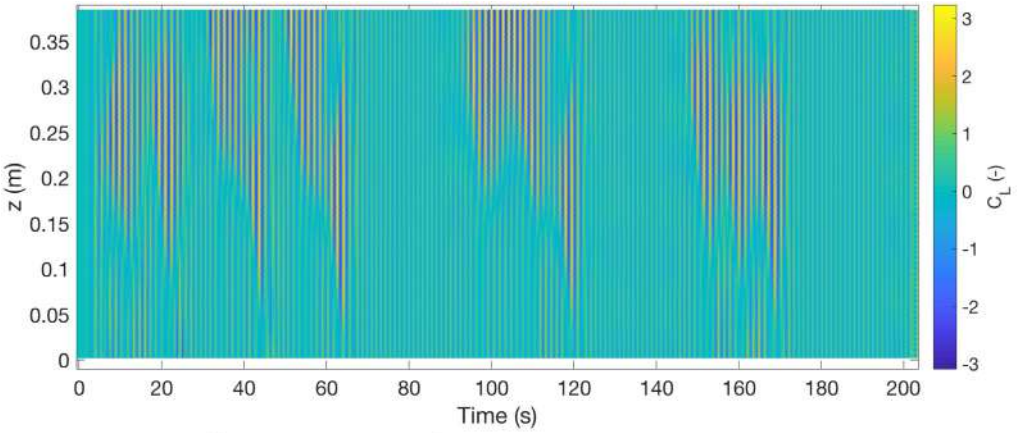

(d) Transition upper/lower branch, Re=5042, U^*=6.00

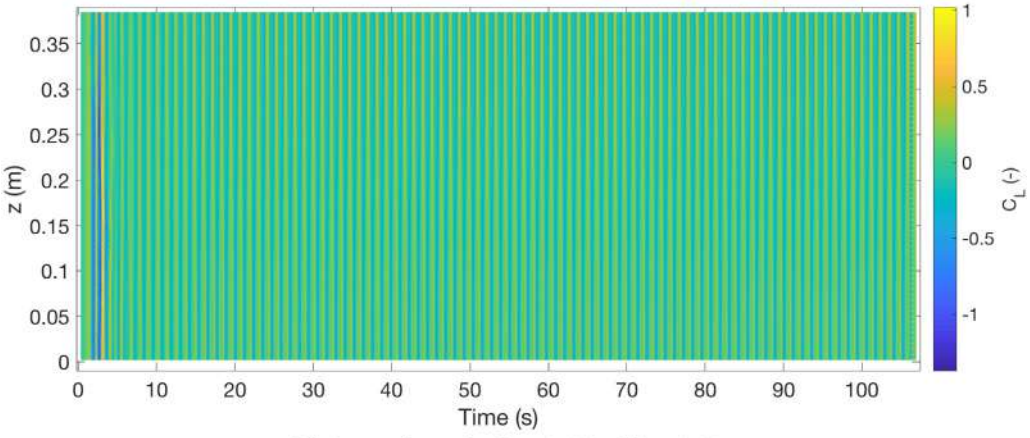

(e) Lower branch, Re=8404, U^*=10.00

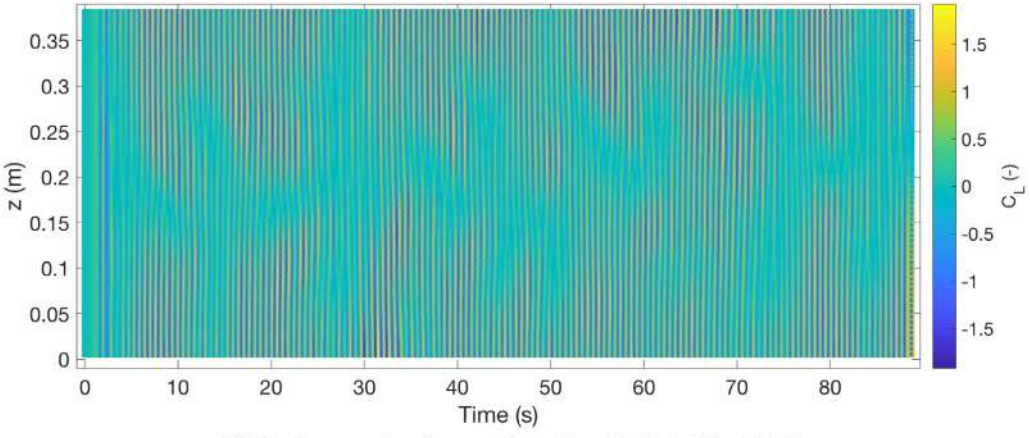

(f) Deshyncronization regime, Re=10084, U^*=12.00

Fig. 7. (*continued*).

intermittent switching is shown using the Hilbert transform (Fig. 6(f) bottom right), where the upper branch region is characterized by lower frequencies, while higher frequencies are associated to the lower branch. The switching between upper and lower branches is highlighted by the total phase ϕ jump between 0 and 180 deg. In the lower branch, the total phase ϕ and the vortex phase ϕ_{VS} remains at 180 deg.

From $U^* = 6.25$ (Fig. 6(g)), the correspondence between 2D and 3D cases is restored until the start of the desynchronization regime. From the comparison of the 2D and the 3D results for $U^* = 12$, showed in Fig. 6(h), it can be seen that the 2D solution is periodical, while the 3D case show non-periodic behaviour.

4.3. Wake flow three-dimensionality

Fig. 7 shows the variation of lift force along the cylinder span direction in time for different response branches. The strongest variation of the sectional lift force along the span direction occurs in the transition zones. For example, at $U^* = 5$ and 6 (shown in Fig. 7(b) ad Fig. 7(d) respectively) the sectional lift force shows considerable variation along the cylinder span.

For $U^* > 11$, the three-dimensionality of the flow is well developed. For example, in the case of $U^* = 12$ (Fig. 7(f)) the forces are not synchronized along the span, leading to a more irregular cylinder motion. The strong three-dimensionality in the wake produces smaller excitation forces with respect to the cases with lower inflow velocities, this leads to a consequent reduced oscillation amplitudes of the cylinder. The wake flow is found to be almost bi-dimensional in the initial branch (Fig. 7(a)), at resonance in the upper branch (Fig. 7(c)) and in the lower branch (Fig. 7(e)).

Fig. 8 shows the three-dimensional representations of the lift coefficient C_L as a function of time and space for 5 significant periods of the time series. The surface representation of the lift force coefficient is plotted in order to give a more detailed picture of its span-wise distribution. It may be noted that for the $U^* = 3.5$ case (Fig. 8(a)), although the wake flow in the initial branch is considered bi-dimensional, small span-wise variation of the forcing term are present.

In the upper branch area where peak amplitude response are observed (Fig. 8(c)), 3D effects are not visible in the lift force distribution. The lower branch also shows no variation of the lift coefficient along the cylinder span, e.g. $U^* = 7.50$ (Fig. 8(d)). This results are in contrast with the previous founding of Zhao et al. (2014), where the three-dimensionality of the flow were found to be the strong both in the upper branch and in the lower branch. One of the possible reason behind this discrepancy could be that in the simulations made by Zhao et al. the Reynolds number was kept at a constant value of 1000, and the mechanical parameters were changed in order to obtain increasing reduced velocities.

When the desyncronization regime starts at $U^* \approx 10$, the three-dimensional disturbances in the wake flow heavily impact on the lift coefficient distribution (Fig. 8(f)), as expected.

As suggested by Zhao et al. (2014) the variation of the lift coefficient along the cylinder span can be quantified by the *correlation coefficient* between two locations at z_1 and z_2 along the cylinder span, which is defined by

$$R(z_1, z_2) = \frac{\overline{C_L(z_1)C_L(z_2)}}{[C_{L,\mathrm{rms}}(z_1)C_{L,\mathrm{rms}}(z_2)]},$$

where the over-bar stands for averaging over the time. Fig. 9 shows the variations of the correlation coefficient R(0,z) of the sectional lift coefficient with z. R(0,z) represents the correlation coefficient of the lift coefficient between one end of the cylinder at $z = 0$ and the considered section. It is evaluated considering the last 10 oscillations of the cylinder. It can be seen that the correlation of the lift coefficient stay close to 1 in the upper and lower branch. This indicates that there are no three-dimensional effects. Even if slight variations are present, the cases in the initial branch can also be considered bi-dimensional.

The three-dimensional character of the wake field can be visualized more detail using the λ_2 method proposed bu Jeong and Hussain (1995) in which λ_2 is the second eigenvalue of the symmetric tensor $E^2 + \Omega^2$. Here E and Ω are the symmetric and anti-symmetric parts of the velocity gradient tensor $\nabla\mathbf{u}$.

Fig. 10 and Fig. 11 show the $\lambda_2 = -0.2$ iso-surfaces. The iso-surfaces are coloured according to the spanwise components of vorticity $W_z = \partial u_y/\partial x - \partial u_x/\partial y$ and the streamwise component of vorticity $W_x = \partial u_z/\partial y - \partial u_y/\partial z$ respectively.

In Figs. 10(a)–10(b), the three-dimensional distortion of the vortex tubes in the initial branch ($2 < U^* < 4$) can be seen.

This is due to the presence of pairs of counter-rotating, rib-like structures of streamwise vorticity braided together with the span-wise vortices. However, the intensity of the rib vortices is too weak to influence the primary mode of vortex shedding for the case $U^* = 2.5$ and $U^* = 3.5$ (Fig. 10b). Consequently, also the cylinder motion response is not altered and remains essentially identical to that obtained from the bi-dimensional computations. On the contrary, in the case $U^* = 3.0$ (Fig. 10a), the rib structures close to the cylinder disrupt the wake. This causes a variation in the response of the cylinder both in terms of motion amplitude and its dominant frequency (Figs. 4(a) and 4(b)).

The intensity of the three-dimensional structures are also evident during the transition between initial and upper branch (Fig. 10(c)).

In the upper branch region, the wake vortex formations appear to be bi-dimensional (Fig. 10(d)). In the lower branch, the three-dimensionality of the flow is very weak and is restricted to the initial transitory. This is clearly evident in figures Fig. 10(e) and Fig. 11(e), for instance, by the fact that the streamwise vorticity W_x disappears. Therefore, the lower branch exhibits mostly bi-dimensional mode characteristics.

For $U^* > 10$ (Figs. 10(f) and 10(g)), the three-dimensional distortion of the vortex tubes becomes important. This, in terms, forms a complex vortex structure generated from the interaction between the von Karman street vortexes and longitudinal rib vortexes.

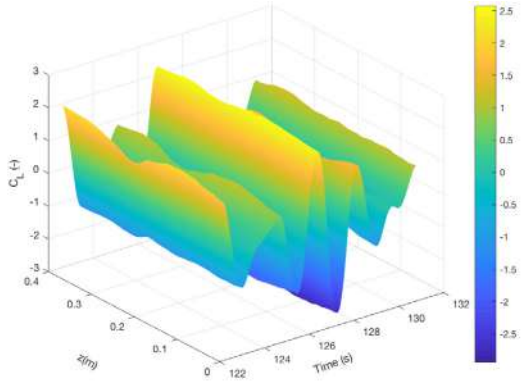

(a) Initial branch, Re=2941, U^*=3.50

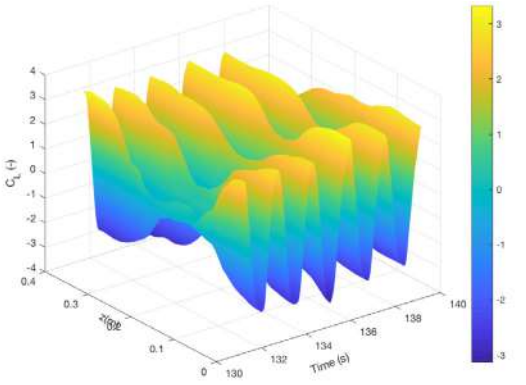

(b) Upper branch, Re=4202, U^*=5.00

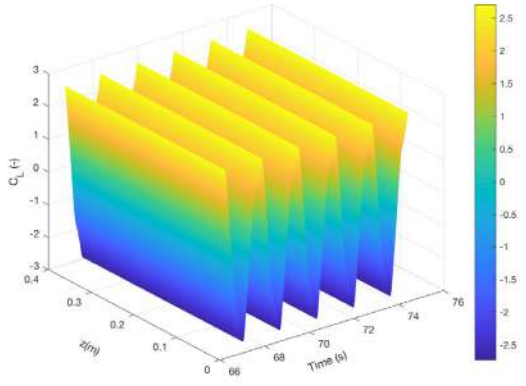

(c) Upper branch, Re=4622, U^*=5.5

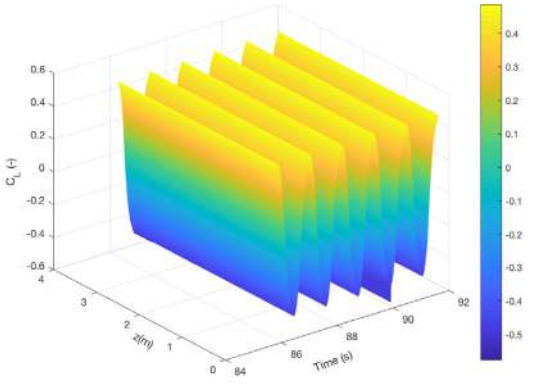

(d) Lower branch, Re=6303, U^*=7.50

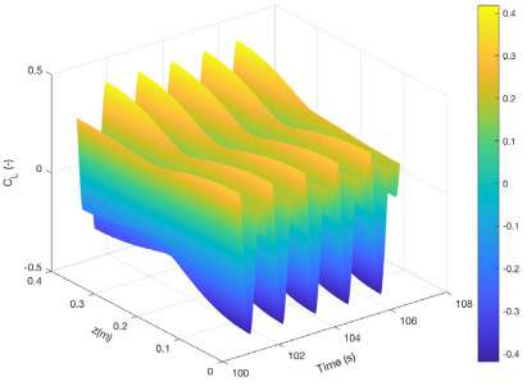

(e) Lower branch, Re=8404, U^*=10.00

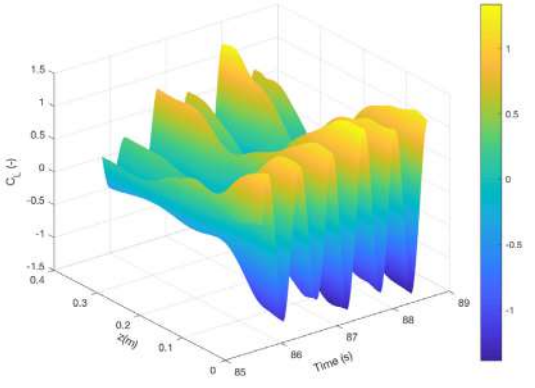

(f) Deshyncronization regime, Re=10084, U^*=12.00

Fig. 8. 3D plot of the span-wise distribution of the lift coefficient for the 3D URANS cases.

4.4. Vortex shedding modes

Vortex shedding modes, defined by the vortex pattern observed in cylinder wake flow are also investigated in the present work. The axial vorticity field W_z is plotted for the three branches of cylinder response in Fig. 12 and Fig. 13

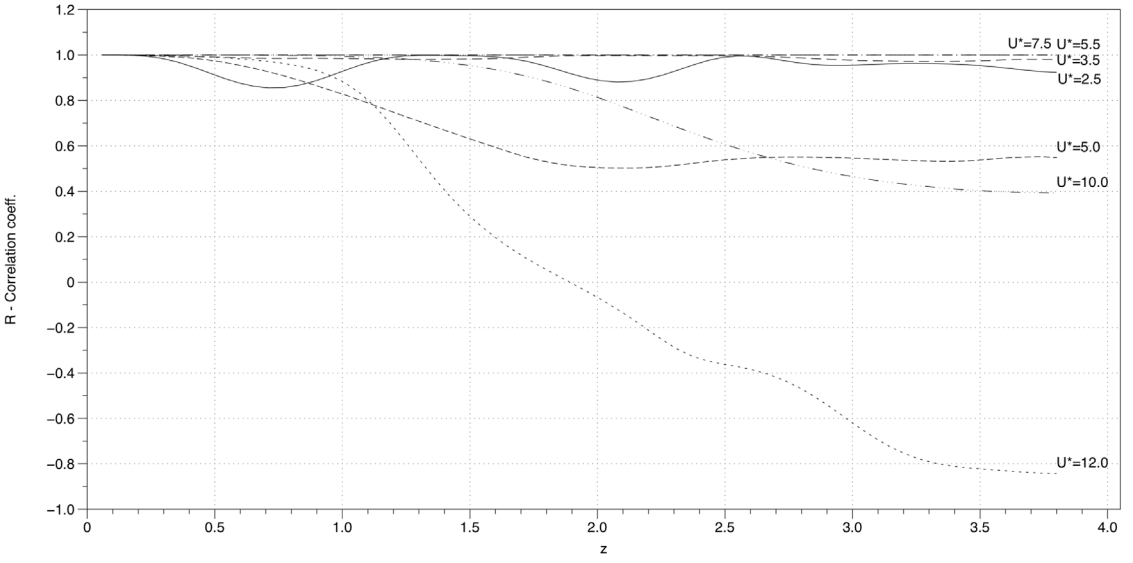

Fig. 9. Correlation coefficient R(0,z) of the sectional lift coefficient.

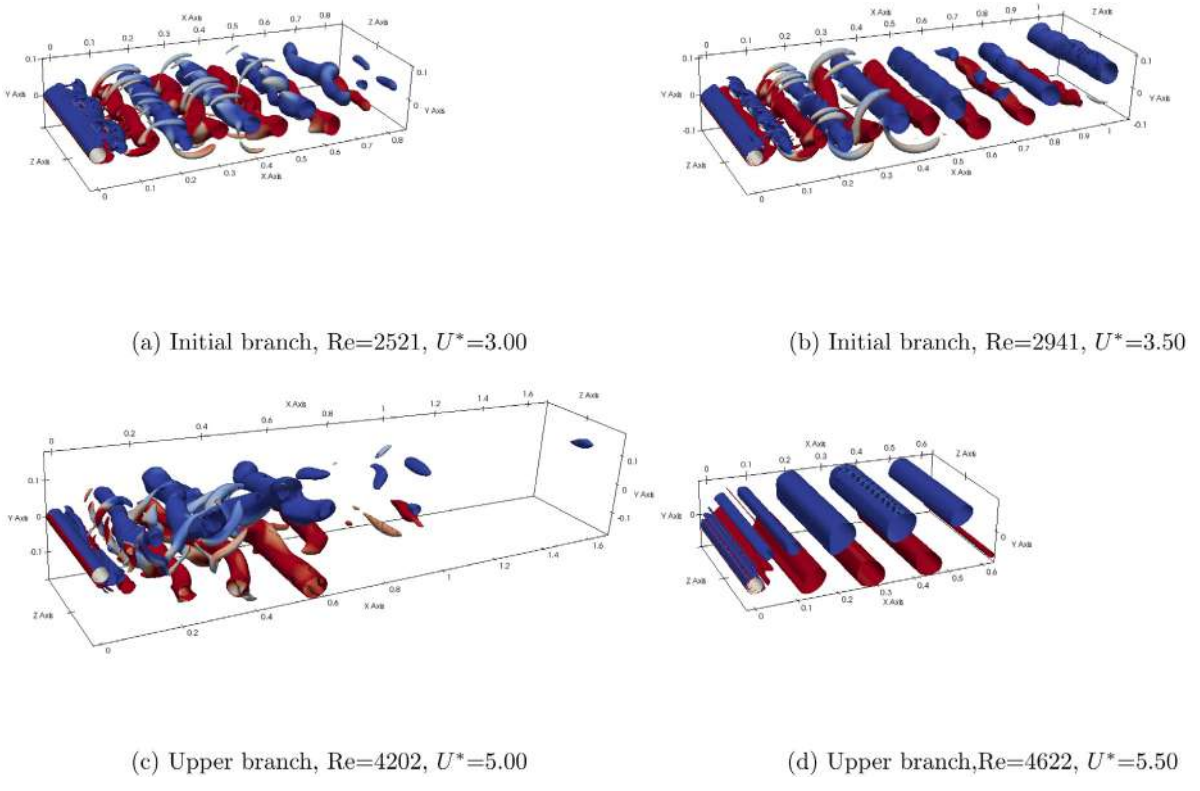

(a) Initial branch, Re=2521, U^*=3.00

(b) Initial branch, Re=2941, U^*=3.50

(c) Upper branch, Re=4202, U^*=5.00

(d) Upper branch,Re=4622, U^*=5.50

Fig. 10. Iso-surface of the eigenvalue $\lambda_2 = -0.2$ and the contours of span-wise vorticity W_z for the 3D URANS cases (blue: clockwise, red: anti-clockwise). (For interpretation of the references to colour in this figure legend, the reader is referred to the web version of this article.)

for the 2D and the 3D cases, respectively. The vorticity plots in Figs. 12 and 13 are relative to the lowest position of the cylinder trajectory. In order to better observe the pattern variations along the axial direction of the cylinder, the figures referring to the 3D RANS simulations (Fig. 13) show three different sections of cylinder. In order to provide a comparison with literature, the CFD results are plotted against the Williamson–Roshko map (Williamson and Roshko, 1988). As suggested by Khalak and Williamson (1999), the adimensional amplitudes A^* are plotted as a function of the

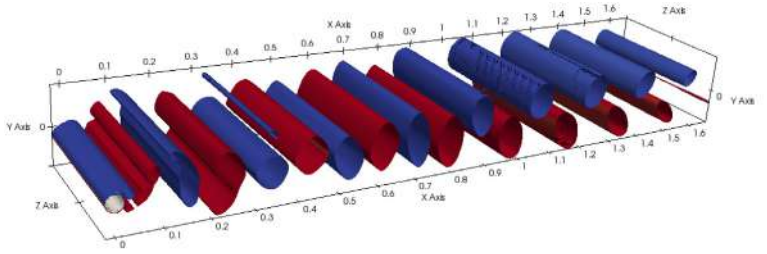

(e) Lower branch, Re=5882, U^*=7.00

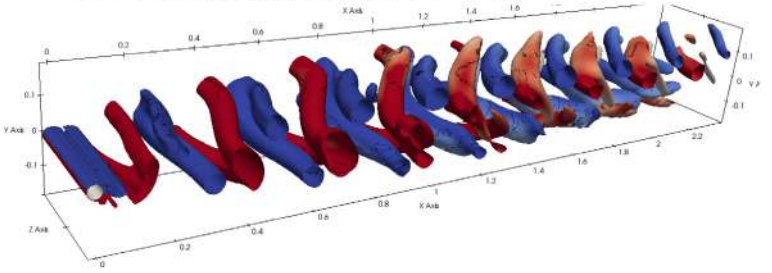

(f) Lower branch, Re=8404, U^*=10.00

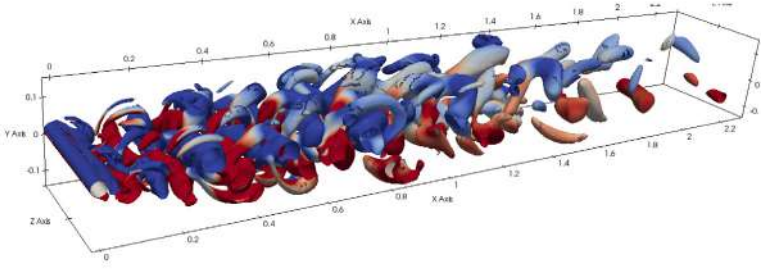

(g) Deshyncronization regime, Re=10084, U^*=12.00

Fig. 10. (*continued*).

so called "true" reduced velocity (U^*/f^*)St (Fig. 14), where St is the Strouhal number (St = 0.2). In general, the vortex shedding modes are similar between the 2D and the 3D cases, however, there are some exceptions. The vortex shedding modes are in good agreement with the Williamson–Rosko map. The 2S vortex shedding mode, that is two single vortices of opposite circulation are shed from the cylinder, is observed in the initial branch (Von karman vortex street) for both 2D (Fig. 12(a)) and 3D 13(a) simulations.

The 2P mode, that is the formation of vortex pairs which convect laterally outwards from the wake centreline, is observed in the upper branch for all cases and in some part of the lower branch. Good agreement has been found between Williamson–Rosko map and the 3D case in the upper branch, e.g. Fig. 13(b) for the case of $U^* = 5.75$. On the other hand, even if the 2D case shows the same vortex pattern of the 3D case (2P), it is barely outside 2P region of the Williamson–Rosko map (Fig. 12(b)). Since the 2P/2S transition is subject to hysteretic effects, both states are possible near the boundary line, as shown in Williamson and Roshko (1988), this could easily be the case. The transition from upper to lower branches also characterized by the vortex shedding mode transition, from 2P to 2S. In Both 2D (Figs. 12(c)–12(d)) and 3D (Figs. 13(c)–13(d)), it can be observed change in the vortex pattern. This is also shown when the data points are plotted on the Williamson–Rosko map (Fig. 14). As the inflow velocity increases, the vortex pattern again change from 2S to 2P. This transition is clearly observed by comparing Figs. 12(d)–13(d) for the case of $U^* = 6.25$ and Figs. 12(e)–13(e) for the case of $U^* = 9$. This vortex pattern change is again in accordance with the Williamson–Rosko map. Finally, when U^*

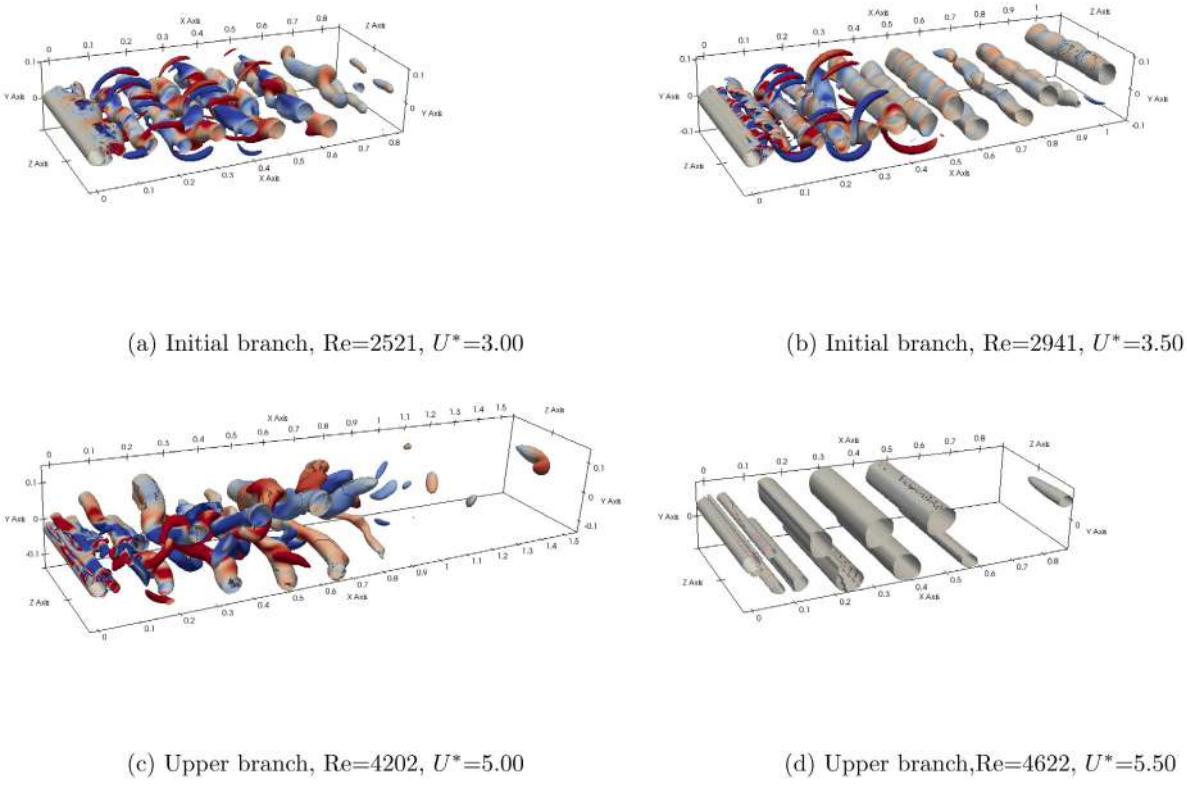

(a) Initial branch, Re=2521, U^*=3.00

(b) Initial branch, Re=2941, U^*=3.50

(c) Upper branch, Re=4202, U^*=5.00

(d) Upper branch,Re=4622, U^*=5.50

Fig. 11. Iso-surface of the eigenvalue $\lambda_2 = -0.2$ and the contours of the stream-wise vorticity W_x for the 3D URANS cases (blue: clockwise, red: anti-clockwise). (For interpretation of the references to colour in this figure legend, the reader is referred to the web version of this article.)

exceeds the limit of the periodic 2P mode, the numerical solution follows the expected drop in amplitude ratio A^* going into the desynchronization regime. This final region is identified with "no observed synchronization pattern" in Fig. 14, meaning that no wake pattern having the same period as the oscillation was observed. Wake flow of both 2D (Fig. 12(f)) and 3D cases (Fig. 13(f)) show the absence of a recognizable pattern.

4.5. Computational costs

Every simulation, has been carried out on the same workstation, a Tier-1 Linux Cluster (Intel® Xeon® E5-2680 v2 CPU).

The cluster is based on IBM Dataplex dx360 M4 servers made by 224 nodes and 4480 cores. The total RAM of the cluster is 12TB with 2GB per core for most of the nodes, 8GB per core for 24 nodes and 16GB per core for 8 special nodes. The interconnection between the nodes is provided by an Infiniband QDR (40Gbit/s) network.

The execution time of a 2D case, parallelized via Open Message Passing Interface (MPI) in 8 different processes in the same computing node, was 2 h and 19 min for 200 s of simulated time for $U^* = 6$. The same case with a three-dimensional mesh, parallelized in 120 processes divided in 6 different computing nodes, took was 6 days 11h and 16 min for the same simulated time.

At higher reduced velocities, the execution time grows in proportion to the decrease in the time step, requiring an even larger number of steps to compute the same amount of simulated time. Therefore, despite a considerable increase in computational resources, the three-dimensional numerical simulation of a single case is not practical for engineering design purposes.

5. Conclusions

The results of 2D and 3D numerical simulations of Vortex Induced Vibrations (VIV) of an elastically-mounted circular cylinder, with low mass ratio and damping ratio, have been compared successfully to experimental data from the literature.

The aim of the study was to investigate the difference between the 2D and 3D numerical simulations in the case of 1-DOF VIV using a simple URANS approach in order to investigate the limits of the simpler approach. It has been

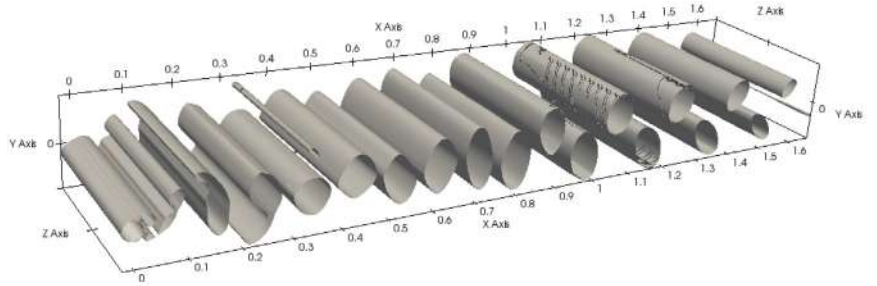

(e) Lower branch, Re=5882, U^*=7.00

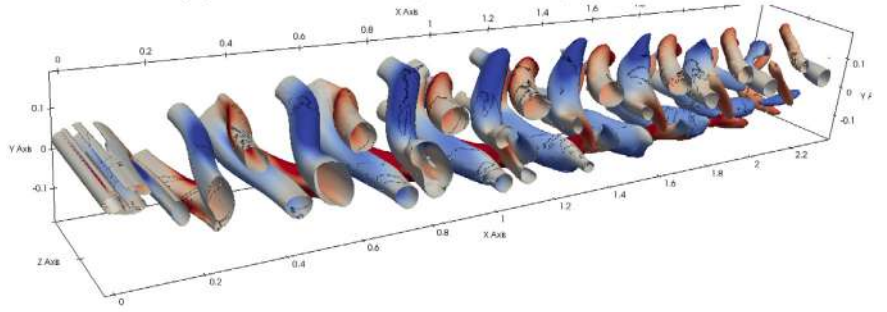

(f) Lower branch, Re=8404, U^*=10.00

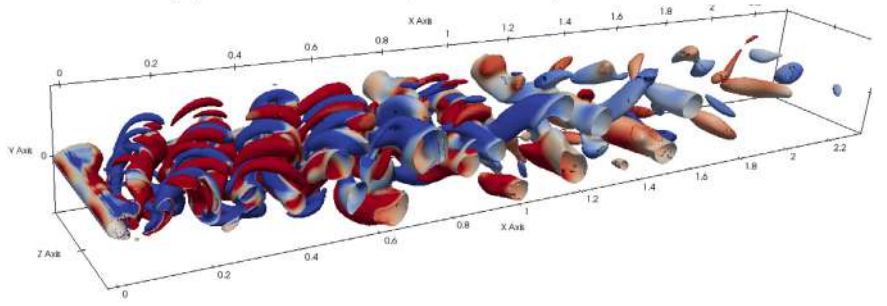

(g) Deshyncronization regime, Re=10084, U^*=12.00

Fig. 11. (*continued*).

found that the bi-dimensional simulations did not show important discrepancies with the experiments except for the non-dimensional amplitude of the cylinder motion in the upper branch region. In order to overcome such issues, more computationally expensive three-dimensional simulations have been carried out. The analysis of the phase between the cylinder response and the fluid forces confirms that the transition between the upper and lower is associated with the phase jump ϕ between the cylinder motion and the total force.

On the other hand, it is not clear if the phase jump ϕ_{VS} between the cylinder oscillation and the vortex shedding force could be the cause of the transition between the initial branch and the upper branch as it is not shown in our 3D simulations results.

The main difference between the 2D and 3D simulation in the upper branch region are due to the different phase between the vortex shedding force and the cylinder motion and are not related to three-dimensional flow structures.

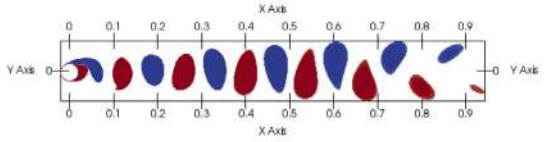

(a) Initial branch, Re=2101, U^*=2.50, $(U^*/f^*)\mathrm{St} = 0.837$

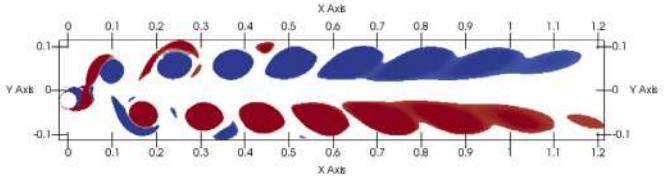

(b) Upper branch, Re=4832, U^*=5.75, $(U^*/f^*)\mathrm{St} = 0.907$

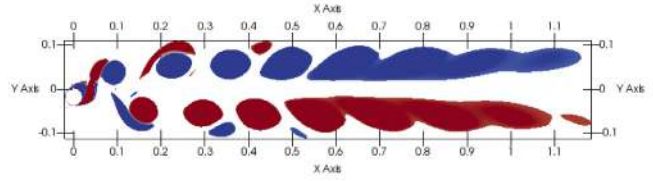

(c) Transition upper/lower branch, Re=5042, U^*=6.00, $(U^*/f^*)\mathrm{St} = 0.902$

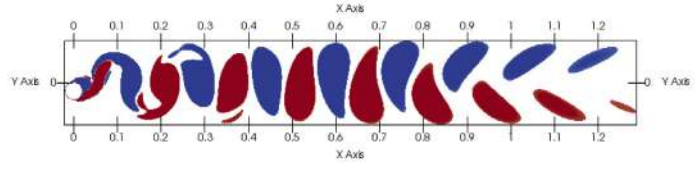

(d) Lower branch, Re=5252, U^*=6.25, $(U^*/f^*)\mathrm{St} = 0.930$

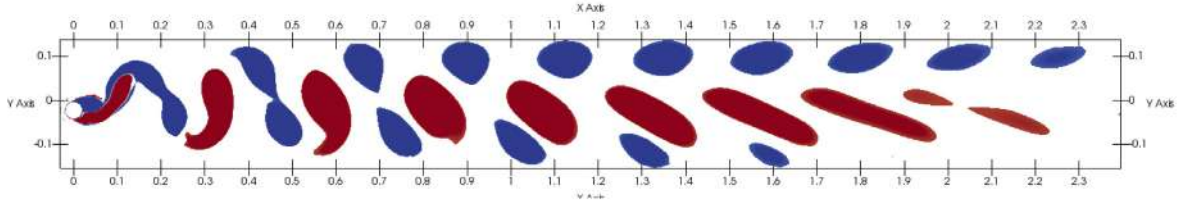

(e) Lower branch, Re=7563, U^*=9.00, $(U^*/f^*)\mathrm{St} = 1.390$

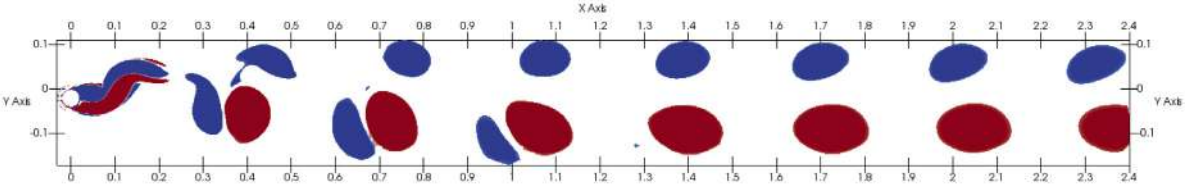

(f) Deshyncronization regime, Re=10084, U^*=12.00, $(U^*/f^*)\mathrm{St} = 1.797$

Fig. 12. Contour of the axial vorticity W_z for the 2D URANS cases (blue: clockwise, red: anti-clockwise). (For interpretation of the references to colour in this figure legend, the reader is referred to the web version of this article.)

From the analysis of the wake flow in span-wise direction it was found that the three-dimensionality of the flow is stronger in the transition zones. The best comparison with the bi-dimensional case was found in the lower branch were

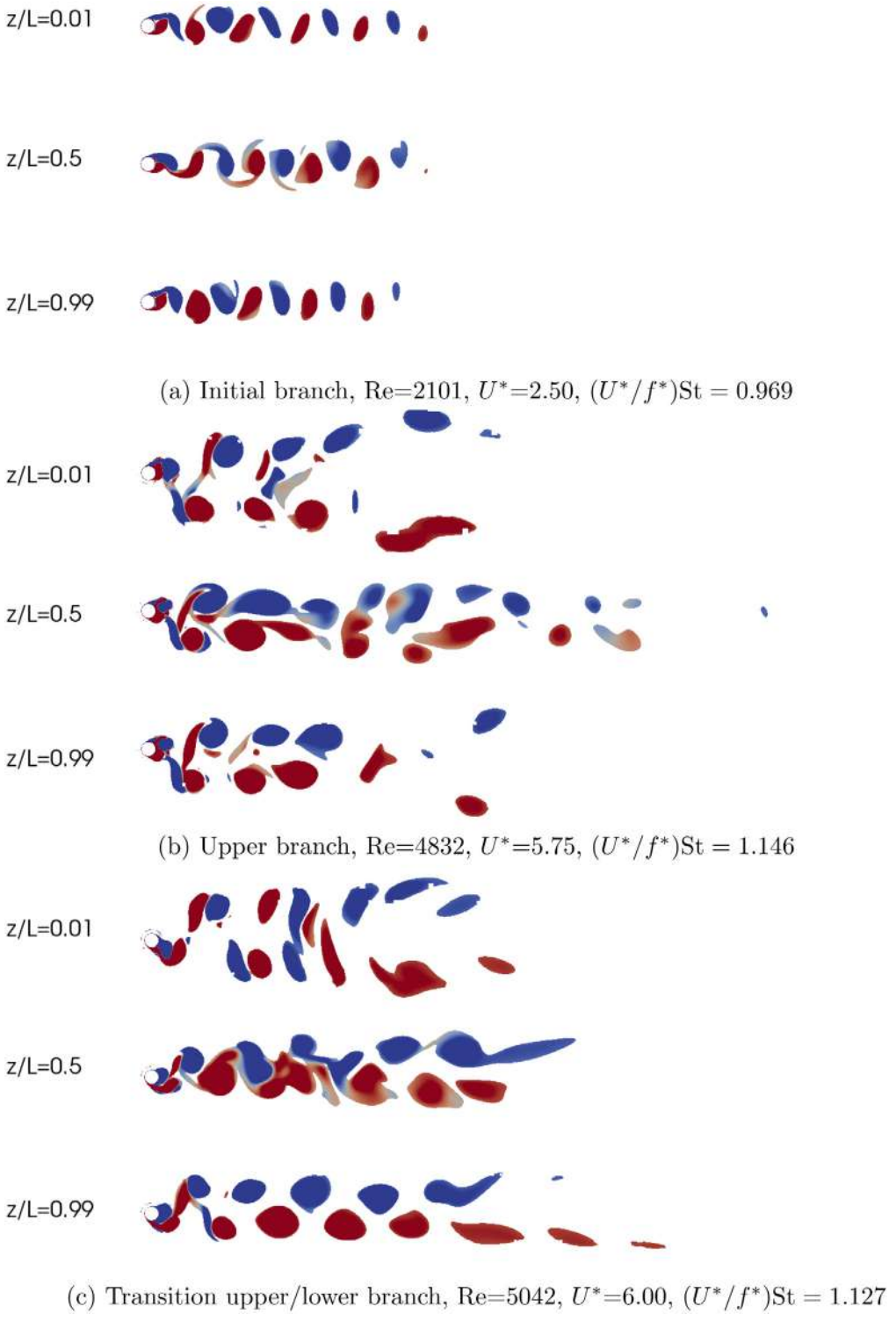

Fig. 13. Contour of the axial vorticity W_z at three section along the cylinder span for the 3D URANS cases (blue: clockwise, red: anti-clockwise). (For interpretation of the references to colour in this figure legend, the reader is referred to the web version of this article.)

three-dimensional flow effects are absent. The visualization of the wake velocity field agrees the vortex shedding modes of the Willamson–Rosko map.

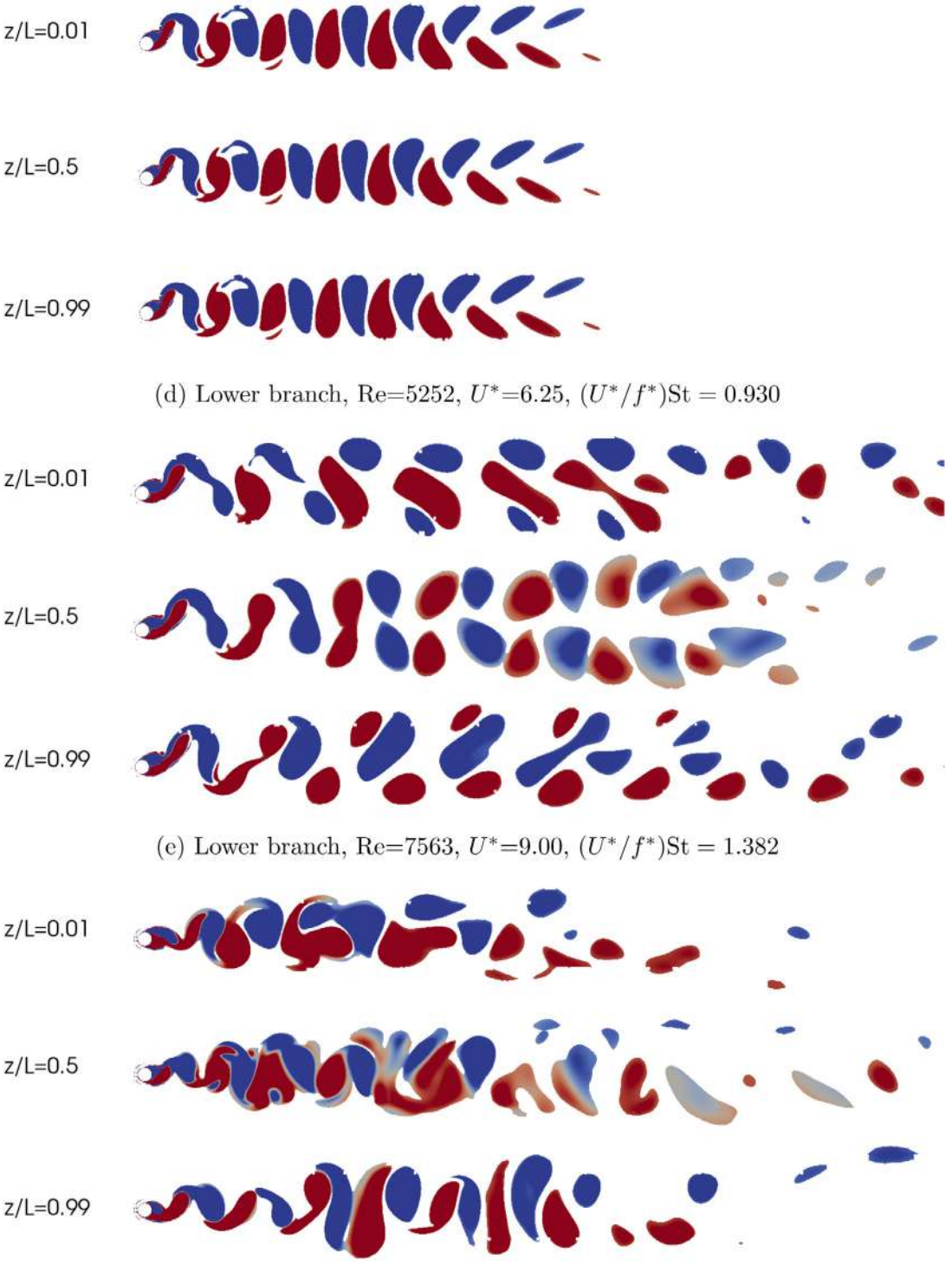

(d) Lower branch, Re=5252, U^*=6.25, $(U^*/f^*)\mathrm{St} = 0.930$

(e) Lower branch, Re=7563, U^*=9.00, $(U^*/f^*)\mathrm{St} = 1.382$

(f) Deshyncronization regime, Re=10084, U^*=12.00, $(U^*/f^*)\mathrm{St} = 1.777$

Fig. 13. (*continued*).

One of the reasons behind the differences between the present results and experiments could be due to the inability of $k-\omega$ SST URANS simulations of resolving smaller span and streamwise vortical structures, as already highlighted by Shur et al. (2005).

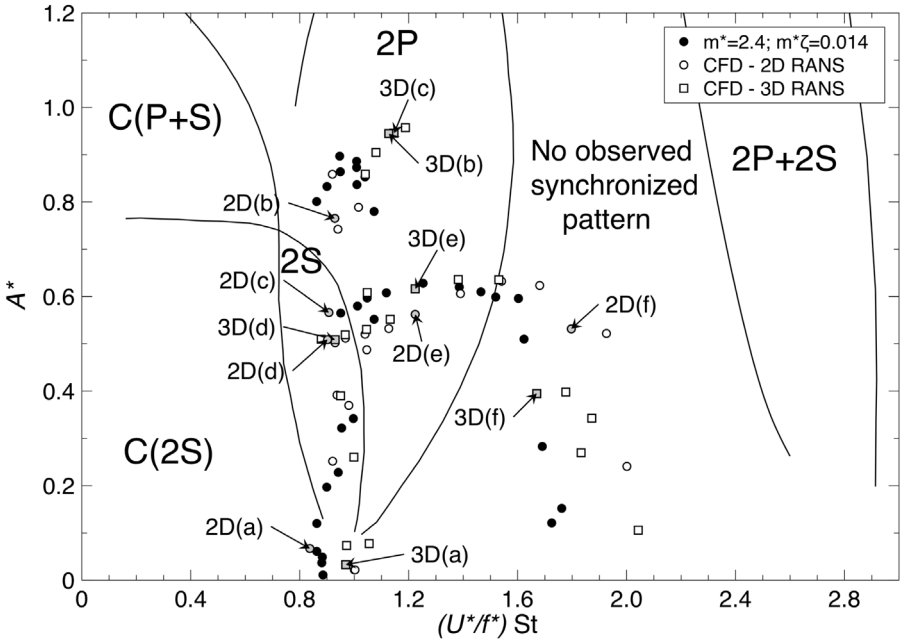

Fig. 14. After Khalak and Williamson (1999). Amplitude response is plotted against the "true" normalized velocity (U^*/f^*)St of all CFD cases plotted in the Williamson and Roshko (1988) map of the vortex shedding modes. Grey-filled data points refer to cases shown in Fig. 12 (2D) and Fig. 13 (3D).

In this regard, the use of more advanced SAS, DES or LES methodologies to investigate the subject are planned.

CRediT authorship contribution statement

Simone Martini: Conceptualization, Methodology, Investigation, Software, Data curation, Writing - original draft, Writing - review & editing. **Mitja Morgut:** Conceptualization, Methodology, Writing - review & editing. **Riccardo Pigazzini:** Conceptualization, Methodology, Writing - review & editing.

Declaration of competing interest

The authors declare that they have no known competing financial interests or personal relationships that could have appeared to influence the work reported in this paper.

Acknowledgments

This work was performed in the context of the UBE 2 (Underwater Blue Efficiency2) project supported by the Regional Program POR FESR 2014 2020, 1.3.b – Bando DGR 1489/2017, Ricerca e sviluppo – Aree di specializzazione tecnologie marittime e smart health of Regione Friuli-Venezia Giulia, Italy.

We wish to dedicate this paper to the memory of Professor Giorgio Contento. He will be remembered for his passion and commitment to research and teaching.

References

Bearman, P., 2011. Circular cylinder wakes and vortex-induced vibrations. J. Fluids Struct. 27, 648–658.

Bernitsas, M.M., Raghavan, K., Ben-Simon, Y., Garcia, E., 2008. VIVACE (Vortex Induced Vibration Aquatic Clean Energy): A new concept in generation of clean and renewable energy from fluid flow. J. Offshore Mech. Arct. Eng. 130 (4), 041101.

Blackburn, H.M., Govardhan, R., Williamson, C., 2001. A complementary numerical and physical investigation of vortex-induced vibration. J. Fluids Struct. 15 (3–4), 481–488.

D. Lucor, G.K., 2005. Vortex mode selection of a rigid cylinder subject to VIV at low mass-damping. J. Fluids Struct. 20, 483–503.

D'Alessandro, V., Montelpare, S., Ricci, R., 2016. Detached–Eddy simulations of the flow over a cylinder at Re=3900 using OpenFOAM. Comput. & Fluids 136, 152–169.

Gabbai, R., Benaroya, H., 2005. An overview of modeling and experiments of vortex-induced vibration of circular cylinders. J. Sound Vib. 282, 575–616.

Govardhan, R., Williamson, C., 2000. Modes of vortex formation and frequency response of a freely vibrating cylinder. J. Fluid Mech. 420, 85–130.

Guilmineau, E., Queutey, P., 2004. Numerical simulation of vortex-induced vibration of a circular cylinder with low mass-damping in a turbulent flow. J. Fluids Struct. 19 (4), 449–466.

Jeong, J., Hussain, F., 1995. On the identification of a vortex. J. Fluid Mech. 285, 69–94.
Khalak, A., Williamson, C., 1996. Dynamics of a hydroelastic cylinder with very low mass and damping. J. Fluids Struct. 10 (5), 455–472.
Khalak, A., Williamson, C., 1999. Motions, forces and mode transitions in vortex-induced vibrations at low mass-damping. J. Fluids Struct. (13), 813–851.
Leontini, J., Thompson, M., Hourigan, K., 2006. The beginning of branching behaviour of vortex-induced vibration during two-dimensional flow. J. Fluids Struct. 22, 857–864.
Löhner, R., Yang, C., 1996. Improved ALE mesh velocities for moving bodies.. Commun. Numer. Methods. Eng. 599–608.
Lysenko, D., Ertesvag, I., Rian, K., 2014. Large-Eddy simulation of the flow over a circularcylinder at Reynolds number 2×10^4. Flow Turbul. Combust. 92 (3), 673–698.
Morse, T., Govardhan, R., Williamson, C., 2008. The effect of end conditions on the vortex-induced vibration of cylinders. J. Fluids Struct. 24 (8), 1227–1239.
Norberg, C., 2003. Fluctuating lift on a circular cylinder: review and new measurements. J. Fluids Struct. 17, 57–96.
Pan, Z., Cui, W., Miao, Q., 2007. Numerical simulation of vortex-induced vibration of a circular cylinder at low mass-damping using RANS code. J. Fluids Struct. 23 (1), 23–37.
Pigazzini, R., Contento, G., Martini, S., Morgut, M., Puzzer, T., 2018b. An investigation on VIV of a single 2D elastically-mounted cylinder with different mass ratios. J. Mar. Sci. Technol. 1–14.
Pigazzini, R., Contento, G., Martini, S., Puzzer, T., Morgut, M., Mola, A., 2018a. VIV Analysis of a single elastically-mounted 2D cylinder: Parameter identification of a single-degree-of-freedom multi-frequency model. J. Fluids Struct. 78, 299–313.
Saltara, F., Neto, A.D., Lopez, J.I.H., 2011. 3D CFD Simulation of vortex-induced vibration of cylinder. Int. J. Offshore Polar Eng. 21 (2), 1–6.
Sarpkaya, T., 2004. A critical review of the intrinsic nature of vortex-induced vibrations. J. Fluids Struct. 19 (4), 389–447.
Shur, M., Spalart, P.R., Squires, K.D., Strelets, M., Travin, A., 2005. Three dimensionality in Reynolds-averaged Navier–Stokes solutions around two-dimensional geometries. AIAA J. 43 (6).
Wanderley, J., Souza, G., Sphaier, S., Levi, C., 2008. Vortex-induced vibration of an elastically mounted circular cylinder using an upwind TVD two-dimensional numerical scheme. Ocean Eng. 35 (14), 1533–1544.
Williamson, C., Govardhan, R., 2004. Vortex-induced vibration. Annu. Rev. Fluid Mech. 36 (423–55).
Williamson, C., Govardhan, R., 2008. A brief review of recent results in vortex-induced vibrations. J. Wind Eng. Ind. Aerodyn. 96, 713–735.
Williamson, C., Roshko, A., 1988. Vortex formation in the wake of an oscillating cylinder. J. Fluids Struct. 2 (4), 355–381.
Wu, W., Bernitsas, M.M., Maki, K., 2014. RANS Simulation versus experiments of flow induced motion of circular cylinder with passive turbulence control at 35,000$<$ RE $<$ 130,000. J. Offshore Mech. Arct. Eng. 136 (4), 041802.
Zhao, M., Cheng, L., An, H., Lu, L., 2014. Three-dimensional numerical simulation of vortex-induced vibration of an elastically mounted rigid circular cylinder in steady current. J. Fluids Struct. 50, 292–311.